UNITED NATIONS EDUCATIONAL, SCIENTIFIC AND CULTURAL ORGANIZATION
INTERNATIONAL ATOMIC ENERGY AGENCY
INTERNATIONAL CENTRE FOR THEORETICAL PHYSICS
I.C.T.P., P.O. BOX 586, 34100 TRIESTE, ITALY, CABLE: CENTRATOM TRIESTE

H4.SMR/984-22

Winter College on Quantum Optics: Novel Radiation Sources

3-21 March 1997

X-ray emission from laser produced plasmas

D. Giulietti

Dipartimento di Fisica, Università di Pisa, Italy

INTERNATIONAL CENTRE FOR THEORETICAL PHYSICS

Winter College on Quantum Optics:
Novel Radiation Sources

(TRIESTE, 3-21 March 1997)

X-ray Emission from Laser Produced Plasmas

Danilo Giulietti

Dipartimento di Fisica, Università di Pisa,
Piazza Torricelli, n.2, 56100, Pisa, Italy

Istituto di Fisica Atomica e Molecolare, C.N.R.,
Via del Giardino, n.7, 56100, Pisa, Italy

Abstract.

In the present paper the laser produced plasmas as ultra bright X-ray sources are presented. The laser absorption is firstly considered and afterwards the main X-ray emission mechanisms. A comparison between the different X-ray sources nowadays available is carried out, as well as a roundup of the main applications of the X-ray from laser produced plasmas.

1. Introduction

Since the first experiments on laser-matter interaction was apparent that laser produced plasmas represented a bright source of electromagnetic radiation in the X-UV spectral region. In fact the electron density of the produced plasmas ($10^{21\text{-}24}$el/cm^3) was of the order of that of the conduction electrons in a metal, while the temperature resulted several order of magnitude higher (0.1-1 KeV). The high values of density and temperature make those plasmas optimal media for an efficient X-ray emission.

Being the laser absorption in these collisional plasmas quite high, the conversion efficiency of the laser energy into X-ray energy is ranging from 1 to 20 %.

The typical X-ray pulses so produced have energy of 0.1 to 10 J, delivered in times of 10^{-12} sec to 10^{-9} sec, up to powers close to 1 TW.

These X-ray sources are very small, in fact their dimensions are those of the focal spots of the focused laser beams (ϕ=10-100μm). So, even if the radiation is emitted in the full solid angle ($\Omega=4\pi$), the source brightness is considerably elevated (up to 10^{17}W/cm^{2}sterad).

Beside the thermal, incoherent X-ray emission the laser plasmas have been recognised as interesting media for the generation of coherent X-ray radiation. Two ways to do that are the high harmonics generation and the inversion of electron population for the achievement of the laser emission conditions.

High harmonics have been generated both in gases and in laser produced plasmas from solid target. In the first case the laser intensity have to be under the ionisation threshold (typically of the order of 10^{12} W/cm^2 for low-pressure noble gases). In fact the physical mechanisms responsible for the high harmonics generation is the anarmonicity of the bound electron oscillation, due to the electric field of the impinging laser radiation. Owing to the inversion symmetry of the potential energy of the electrons in the field of the nucleus of an atomic gas, only the odd harmonics can be generated in gases.

The conversion efficiency rapidly decreases over the 20-30 th harmonics, even if harmonics of order as high as the 100th ($\approx$ 100Å) have been observed for the Nd laser . Even though the intensity of the harmonics is, due to the aforementioned reasons, quite low, the harmonic brightness is high. In fact the divergence of harmonic radiation is decreasing with the number of the order, following the relation $\theta_n=\theta_0 n$. Even more relevant is the spectral brightness, due to the narrow spectral band of the harmonic emission.

Harmonic generation from solid surfaces irradiated with high intensity laser pulses involves plasma formation. In this case even and odd harmonics can be produced.

The laser emission in the X-ray spectral region is one of the more fascinating goals for the scientific community. In fact a lot of relevant applications can be allowed with such an intense and coherent source of X-ray radiation. One between the many, the holography at sub-nanometer scale. However, owing to the large separation of the electronic levels between whose the laser effect has to be produced, the required power to operate the population inversion is so high that can be delivered only by the most powerful laser on the world.

2.Laser produced plasmas.

2.1 Basic concepts in laser-plasma interactions.

Laser radiation of high intensity impinging on solid target, rapidly produces a plasma on his surface. The laser propagation in the plasma is dominated by the presence of free electrons, and follows the dispersion relation:

$$\omega_L^2 = \omega_p^2 + k_L^2 c^2$$

where ω_L and k_L are the frequency and the wave number of the laser light, c is the speed of light in the vacuum and

$$\omega_p = \sqrt{\frac{4\pi n_e e^2}{m}}$$

is the plasma frequency. In the previous equality e and m are the charge and the mass of the electron respectively and n_e is the plasma electron density. The group velocity $v_g = c\sqrt{1-\frac{\omega_p^2}{\omega_L^2}}$ decreases with the electron density, down to the limit value $v_g=0$, for the critical density $n_c = \frac{m\omega_L^2}{4\pi e^2} = \frac{1.1\times10^{21}}{\lambda_L^2(\mu m)} cm^{-3}$. Hereafter the light wave is evanescent. The laser light can not propagate at densities $n_e>n_c$, so the interaction develops in the underdense plasma.

A rough estimate of the temperature of the laser produced plasma can be done by equating the absorbed laser intensity I_{abs} to the electron heat flux

$$I_{abs} \approx f\left(\frac{k_B T_e}{m}\right)^{1/2} n_e k_B T_e,$$

where k_B is the Boltzmann constant and f<1 is a "flux limit". Solving for the temperature we obtain

$$T_e \approx \left(\frac{I_{abs}}{f n_e}\right)^{2/3} \frac{m^{1/3}}{k_B} \approx 3\times10^7 \left(\frac{I_{abs}^{W/cm^2}}{f n_e}\right)^{2/3} eV.$$

For typical plasma parameters $I_{abs}=10^{14}W/cm^2$, f=0.05, $n_e=10^{21}cm^{-3}$, we obtain Te=4.8 KeV.

When the laser radiation impinges on solid target a plasma develops towards the vacuum. The blow-off velocity is roughly equal to the local sound speed:

$$v \approx c_s = \sqrt{\frac{3T_i + ZT_e}{M}} \approx \sqrt{\frac{ZT_e}{M}} \approx 3\times10^7 \left[\left(\frac{Z}{A}\right)\left(T_e^{KeV}\right)\right]^{1/2} cm/\sec$$

where T_i, Z, M and A are respectively the ion temperature, the charge number, the mass and the mass number of the ion. Typical values for the blow-off velocity range from 10^7 to 10^8 cm/sec.

This velocity determine, for short laser pulses, the density scale length of the produced plasma $L_n \equiv n_e/\nabla n_e \approx \min[c_s\tau, \phi]$, where τ and ϕ are respectively the laser pulse length and the focal spot diameter on the target.

The temperature scale length $L_T \equiv T_e/\nabla T_e$ is very long for $n_c<n_c$, due to the high electron thermal conduction in an underdense, hot plasma;while it results extremely short behind the critical density, where a dense, cold plasma connects to the still solid target.

The Debye length,

$$\lambda_D \equiv \left(\frac{K_B T_e}{4\pi n_e e^2}\right)^{1/2} = \left(\frac{v_e}{\omega_p}\right)^{1/2} \approx 7.43\times10^2 \left(\frac{T_e^{eV}}{n_e}\right)^{1/2} cm,$$

v_e being the thermal electron velocity, gives the action range of the electric field of an individual charged particle in the plasma, and sets a lower limit to the space scale of the electron density perturbation. As a consequence of that, electromagnetic and plasma waves can exist in the plasma provided that $K\lambda_D<<1$, where K is the corresponding wave vector.

Another plasma parameter related to the previous one is the number of electrons in the Debye sphere

$$N_D = \frac{4}{3}\pi\lambda_D^3 n_e = 1.72\times10^9 \left(T_e^{eV}\right)^{3/2} n_e^{-1/2}.$$

In fact, have to be $N_D>>1$, in order that the collective behaviour of the plasma particle be apparent.

Finally a parameter for the degree of coupling of the particles in the plasma,

$$\eta = \frac{K_B T_e}{e^2 n_e^{1/3}} = 6.9\times10^6 \frac{T_e^{eV}}{n_e^{1/3}},$$

given by the ratio of the mean kinetic energy, $K_B T_e$, and the Coulomb potential energy, e^2/r, at the average distance between the particles, $(n_e)^{-1/3}$.

For $n_e=10^{21}cm^{-3}$ and T_e=500eV, λ_D=50Å, N_D=600, and η=350.

2.2. Semi-analitical models of plasma production by lasers.

2.3. Hydrodynamic simulations of laser-produced plasmas

Basic phenomena of laser-plasma interactions can be studied by means of numerical simulation. Once suitable approximations have been made, the set of differential equations that describe the motion of plasma can be solved numerically and the main properties of the plasma can be calculated and compared with the experimental ones. The one-dimensional Lagrangian code MEDUSA (Christiansen et al., 1974, Rodgers et al.,1989) will be briefly described here and examples of simulations of real experiments will be given to describe the benefits and the limits of this approach.

Lagrangian co-ordinates

In a hydrodynamic simulation code the plasma is described as a two component fluid, namely electrons and ions, characterized by four main variables, the plasma mass density $\rho(x,t)$, the fluid velocity $u(x,t)$, the electron temperature $T_e(x,t)$, and the ion temperature $T_i(x,t)$. For the specific purpose of describing laser-plasmas, ions behave as non-degenerate perfect gas, while electrons are described either by an ideal gas equation of state (EOS) or by a Thomas-Fermi EOS. The perfect gas may be either non-degenerate or partially degenerate or fully degenerate and a fully ionized plasma is assumed in this case.

For the particular circumstances of plasmas produced by relatively long pulses (up to few nanosecond), a perfect gas equation of state satisfactorily models the plasma generated in the conditions achieved in this interaction regime. In contrast, in the case of shorter laser pulses (down to few picoseconds), a non-ideal electron gas EOS based on the Thomas-Fermi model can be used and degeneracy effects should also be taken into account. Charge neutrality requires that the electron fluid and the ion fluid share the same velocity. In this case, neglecting internal electric and magnetic fields, the equation of motion becomes

$$\rho \frac{du}{dt} = -\frac{dp}{dx}, \qquad (1)$$

where ρ is the mass density and $p = p_i + p_e$ is the hydrodynamic pressure. Finally the motion of the Lagrangian co-ordinate r is determined by the fluid velocity u according to the following equation

$$\frac{dr}{dt} = u(x,t). \qquad (2)$$

Each subsystem is also governed by an *energy equation* which is obtained by balancing the rate at which laser energy enters the subsystem and the rate at which this energy goes into modifications of the thermodynamic and kinetic state according to

$$C_V \frac{dT}{dt} + B_T \frac{d\rho}{dt} + p\frac{dV}{dt} = S, \qquad (3)$$

where S is the rate of energy input per unit mass, $C_V = (\partial U/\partial T)_\rho$ is the specific heat per unit volume, $B_T = (\partial U/\partial \rho)_T$ describes the variation of internal energy due to interaction between particles within the same subsystem, and $U = pV/(\gamma - 1)$ is the internal energy per unit mass. Electrons can exchange energy via thermal conduction, electron-ion collisions, bremsstrahlung emission and laser light absorption, while ions exchange energy via thermal conduction, electron-ion collisions, and viscous shock heating. Energy is exchanged between ions and electrons by means of electron-ion collisions at a rate given by Eq. . Inverse bremsstrahlung absorption of laser light is modelled using the classical coefficients given by Eq. . Thermal conductivity is modelled in terms of the classical Spitzer (Spitzer, 1953) conductivity with the thermal electron flux limited, for high temperature gradients, to the so called free-streaming limit, F_e^{max} according to the following expression

$$\frac{1}{F_e} = \frac{1}{F_e} + \frac{1}{F_e^{max}} \ , \qquad (4)$$

where the electron thermal flux, according to the usual definition, is proportional to the electron temperature gradient, i.e. $F_e = \kappa_e \nabla T_e$.

Hydrodynamic modelling of long scalelength plasma experiments

In the simulation code, a target can be specified by giving atomic number, atomic mass, mass density, thickness and boundary conditions. Laser pulse parameters can be specified including wavelength, pulse-length, intensity, temporal shape and timing relative to the start-time of the hydrodynamic simulation.

Many physical processes can be included and controlled by means of other input logical switches. Resonance absorption can be included specifying the percentage of laser energy that, not absorbed by inverse bremsstrahlung and having reached the critical density layer, if any, is deposited at the critical density layer. Hot electrons can be included by setting the fraction of laser energy absorbed by the plasma via resonance absorption to be converted in hot electron energy. The hot electron temperature will be determined either as a function of the electron temperature at the critical density or as a function of laser

intensity times the square of the laser wavelength. Ponderomotive force of the laser can also be included if required, in the momentum equation. Finally the ionization equilibrium can be calculated by the code using Saha ionization model.

As an illustrative example, we now consider an experiment in which the plasma is pre-formed by irradiating a target consisting of a small disk of Aluminium (400 μm diameter, 500 nm thick). Four laser beams (600 ps FWHM, 1.053 μm wavelength) are superimposed on target, two on each side of the disk, focused in a 600 μm diameter focal spot. In such a configuration the irradiation geometry is symmetric with respect to the plane of the target. Therefore simulations can be performed by assuming a single-side irradiation, with a target thickness equal to half of the original thickness, and keeping fixed the boundary of the target opposite to the laser.

The simulation code calculated temporal evolution of the main hydrodynamic variables including electron and ion temperature, mass density, hydrodynamic velocity and pressure and average ionization relative to each cell in which the plasma is spatially sampled according to the numerical implementation of the Lagrangian scheme. Radiation losses due to bremsstrahlung emission are also accounted for although, for low and medium Z plasma, they were usually found to be negligible.

Our attention is focused on the plasma formation, heating and initial stage of cooling, when intense X-ray emission occurs and can be investigate experimentally by means of X-ray spectroscopy as will be described in the following sections. Fig.1 shows the results of the simulations in terms of the electron temperature and density profiles at the peak of the heating laser pulses in units of eV and cm^{-3} respectively. Taking into account that the critical density at 1.053 μm is $n_{cr} \cong 10^{21}\,cm^{-3}$, Fig.1 shows that, at the peak of the pulse, the plasma is still overdense over a 50μm long plasma column.

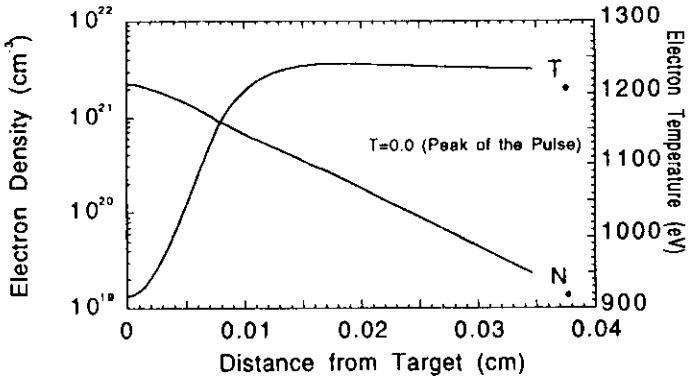

Fig.1. Electron density and temperature profiles obtained from the hydrodynamic simulation at the peak of the heating laser pulse. A 250 nm thick Al target was irradiated at a wavelength of 1.053 μm and at an intensity of 3×10^{13} W/cm^2. The electron conductivity was limited to 10% of the free streaming value.

The electron temperature is predicted to be uniform over the sub-critical region where it is expected to be as high as 1.2 keV, decreasing to approximately 0.8 keV into the higher density region, where laser light cannot propagate. Fig.2 shows the electron temperature and density profiles calculated using the same conditions as in Fig.1 but relative to later times, i.e. 2.2 ns, 3.0 ns and 4.3 ns after the peak of the heating pulse. 2 ns after the peak of the heating pulse the plasma is fully underdense, the peak density being approximately $n_{cr}/10$ and the electron temperature, uniform over the whole plasma, being approximately 600 eV.

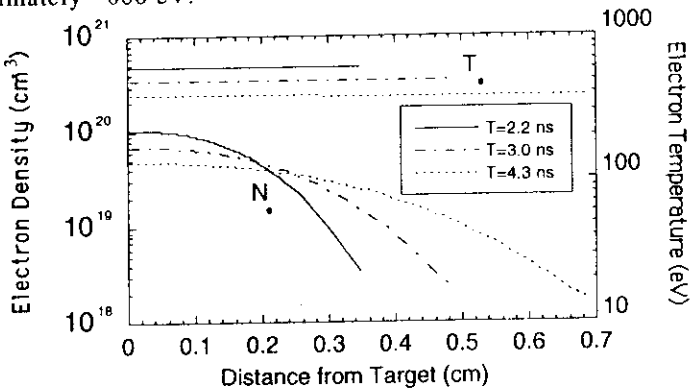

Fig.2. Electron density and temperature profiles obtained from the same simulation of Fig.1 three times after the peak of the heating laser pulse. A 250 nm thick Al disk target was irradiated at a wavelength of 1.053 μm and at an intensity of 3×10^{13} W/cm^2.

3. Laser-plasma interaction mechanisms.

Intense laser radiation, impinging on a solid target, produces a fast ionisation of the atoms at the surface. Later on the radiation is absorbed by different mechanisms.

3.1. Collisional absorption.

The electrons, colliding with the ions under the action of the oscillating laser electric field, transfer the electromagnetic energy to the plasma. The fraction of the absorbed laser radiation propagating in a uniform plasma of length L is:

$$\alpha_{abs} = 1 - \exp(-k_{ib} L)$$

where

$$k_{ib} = 3.1\times10^{-7} Z n_e^2 \ln\Lambda \omega_L^{-2}\left[1-\left(\frac{\omega_p}{\omega_L}\right)^2\right]^{-1/2}\left(T_e^{eV}\right)^{-3/2} cm^{-1}$$

is the imaginary part of the laser wave vector k and

$$\ln\Lambda = 24 - \ln\left(n_e^{1/2}/T_e^{eV}\right)$$

is the Coulomb logarithm.

As one can see, the collisional absorption is strongest for low temperatures, high densities, high Z plasmas. Because a significant fraction of the absorption comes from the region very near the critical density n_c, the absorption is enhanced in the long density scale length plasmas. However there are several processes which can steep the density profile near n_c, so strongly diminishing the inverse Bremsstrahlung absorption(Kruer W.L., 1976).

At high laser intensities the electron-ion collision frequency is modified by the oscillatory motion of the electrons in the laser electric field. In fact the effective electron velocity is

$$v_{eff} = \sqrt{v_e^2 + \left(eE_L/m\omega_L\right)^2}$$

where

$$v_e = \sqrt{\frac{K_B T_e}{m}} = 4.19\times10^7\left(T_e^{eV}\right)^{1/2} cm/\sec$$

and E_L are respectively the electron thermal velocity and the laser electric field. As a consequence of the reduction of the electron-ion collision cross-section,

$$\sigma_{ei} \approx 4\pi Z^2 e^4 m^{-2} v_e^{-4}$$

that scales as v_e^{-4}, the inverse Bremsstrahlung coefficient reduces to the effective value

$$k_{ib}^{eff} = k_{ib}\left[1+\frac{3}{2}\left(\frac{v_E}{v_e}\right)^2\right]^{-1}$$

where

$$v_E = \frac{eE_L}{m\omega_L} \approx 25\lambda_{\mu m}\left(I_{W/cm^2}\right)^{1/2} cm/\sec$$

is the electron quiver velocity, λ and I being respectively the laser wavelength and intensity.

Another cause of reduction of the collisional absorption is due to the non Maxwellian electron distribution that produces for very high laser irradiances (Langdon A.B., 1980). In fact when the rate of the energy gain of an electron from the laser ($\approx \nu_{ei} v_E^2$) is larger than the rate the electron can share energy with other electrons ($\approx \nu_{ee} v_e^2$) to form a Maxwellian, i.e.

$$Z\left(\frac{v_E}{v_e}\right)^2 > 1$$

there is a lack of low-energy electrons in the distribution compared with a Maxwellian. Because the low velocity electrons are the main responsible for the collisional absorption, this consequently reduces. In the previous expressions

$$\nu_{ei} = 3\times10^{-6} Z n_e \ln\Lambda\left(T_e^{eV}\right)^{-3/2}\sec^{-1}$$

and

$$\nu_{ee} \approx \nu_{ei}/Z$$

are respectively the electron-ion and the electron-electron collision frequency.

3.2. Ion turbulence absorption.

The value of the inverse Bremsstrahlung absorption coefficient, reported in 3.1, has been evaluated supposing a completely random ion motion. However, has been showed (Dawson J., 1963) that in the case of correlated motion of the ions, the absorption coefficient can sizeably increase with respect to the classical one.

Considering a coherent ion turbulence with fluctuation spectrum $\delta n_i(\bar{k})$, the energy damping rate of laser radiation becomes

$$\nu_{eff} = \frac{\omega_L}{2}\sum_{\bar{k}}\left(\frac{\delta n_i(\bar{k})}{n_c}\right)^2 \mathrm{Im}\left[\frac{1}{\varepsilon(\bar{k},\omega_L)}\right]\cos^2(\theta_i)$$

where θ_i is the angle between the wave vector k and the laser electric field E_L, and $\varepsilon(\bar{k},\omega_L)$ is the complex dielectric constant of the plasma.

Ion-acoustic fluctuations can cause an increased absorption that, under ideal conditions, might add up to 20% to the total absorption for short pulse (τ<100ps) experiment. For long pulse experiments, ion turbulence absorption can exceed the inverse Bremsstrahlung for low Z targets and λ_L >1μm.

3.3. Parametric instabilities.

When the laser radiation impinges on large regions of underdense plasma with L>λ_L, many physical processes can develop, producing electron and ion plasma waves and stimulated laser scattering. The damping of the waves produces plasma heating, while the scattering strongly reduces the laser absorption in the plasma. Self-focusing and filamentation of the laser radiation, locally enhancing the electromagnetic intensity, make easier to achieve the instability threshold conditions.

Stimulated Brillouin Scattering (SBS). Laser radiation, propagating in undercritical plasmas of long density scale length, produces a transverse current $\propto \delta n \bar{E}_L$, acting on an original low-frequency density perturbation

δn. So, a reflected light wave is produced that, interfering with the incident light, produces a variation in the wave pressure, $\overline{\nabla}\left(\frac{\overline{E}_L \cdot \overline{E}_B}{4\pi}\right)$, which can in turn reinforce the density fluctuations. By this feed-back loop an instability develops, provided that the frequency and wave number matching conditions are satisfied:

$$\omega_L = \omega_B + \omega_i$$
$$\overline{k}_L = \overline{k}_B + \overline{k}_i$$

where (ω_L, k_L), (ω_B, k_B), (ω_i, k_i) are respectively the angular frequency and the wave vector of the impinging laser radiation, the scattered radiation and the ion plasma wave.

In the most relevant case of the backward SBS, developing in a well underdense plasma,

$$\omega_L \gg \omega_B$$
$$\overline{k}_L // -\overline{k}_B,$$

we have, from the matching conditions:

$$k_i \approx 2k_L \approx 2\frac{\omega_L}{c}$$
$$k_B \approx -k_L \approx -\frac{\omega_L}{c}$$
$$\omega_B = \omega_L - 2k_L c_s = \omega_L - 2\omega_L \frac{c_s}{c}$$

SBS can cause large premature reflection of the incident laser radiation before reaching the critical density, so strongly reducing the plasma heating.

Stimulated Raman Scattering (SRS). The physical mechanisms of the Raman instability is very similar to that of the SBS. The laser radiation, propagating through a plasma, whose density is rippled by the density fluctuation δn_e associated with an electron plasma wave, generates a transversal current $\propto \overline{E}_L \delta n_e$. If the wave number and frequency matching conditions are fulfilled

$$\omega_L = \omega_R + \omega_e$$
$$\overline{k}_L = \overline{k}_R + \overline{k}_e$$

this transversal current generates a scattered radiation, which in turn, interfering with the incident laser radiation, reinforces the density fluctuations, via the wave pressure $\overline{\nabla}\left(\frac{\overline{E}_L \cdot \overline{E}_R}{4\pi}\right)$. This positive feed-back produces an instability. The wave number and frequency matching conditions can only be satisfied for densities $n_e < n_c/4$.

From the first of the above reported matching condition and the electron plasma wave dispersion relation

$$\omega_e^2 = \omega_p^2 + 3v_e^2 k_e^2 = \omega_p^2\left[1 + 3\lambda_D^2 k_e^2\right]$$

one gets the frequency shift of the scattered radiation

$$\frac{\omega_R - \omega_L}{\omega_L} = -\left(\frac{n_e}{n_c}\right)^{1/2}\left[1 + 3\lambda_D^2 k_e^2\right]^{1/2}.$$

Using both matching conditions and the dispersion relations of the two electromagnetic waves and of the plasma wave, one can gets the wave vector of the plasma wave, in the condition of weak damping, $k_e\lambda_D \ll 1$:

$$\frac{k_e}{k_L} = 1 \pm \left(\frac{1 - 2N^{1/2}}{1 - N^{1/2}}\right)^{1/2},$$

where $N = n_e/n_c$, and +,- refer respectively to the backward and forward SRS.

Two-Plasmon Decay (TPD). Near the quarter critical density, $n_e = n_c/4$, laser radiation can decay into two electron plasma waves (plasmons) (Giulietti D., 1991) The pair of plasma waves satisfies the energy and momentum conditions

$$\omega_L = \omega_B + \omega_R$$
$$\overline{k}_L = \overline{k}_B + \overline{k}_R,$$

with dispersion relations for photons and plasmons

$$\omega_L^2 = \omega_p^2 + k_L^2 c^2$$
$$\omega_{B,R}^2 = \omega_p^2 + 3k_{B,R}^2 v_e^2,$$

where ω_B, ω_R are the plasmon frequencies and k_B, k_R their wave vectors. In the limit of weak Landau damping of the electron waves, $\overline{k}_{B,R}^2 \lambda_D^2 < 0.1$, one gets

$$\omega_p \approx \frac{\omega_L}{2}\left(1 - \frac{3}{4}\left(k_B^2 + k_R^2\right)\lambda_D^2\right),$$

from which we obtain for the electron density

$$\frac{n_e}{n_c} \approx \frac{1}{4}\left(1 - \frac{3}{2}\left(k_B^2 + k_R^2\right)\lambda_D^2\right).$$

The minimum electron density for TPD is determined by the Landau damping, $k_{B,R}^2 \lambda_D^2 \approx 0.1$, whereas the maximum density is given by the minimum value for $\left(k_B^2 + k_R^2\right)$, which is roughly k_L^2. Consequently the density range for TPD to occur is

$$\left(\frac{n_e}{n_c}\right)_{min} \approx 0.19,$$
$$\left(\frac{n_e}{n_c}\right)_{max} \approx \frac{1}{4}\left(1 - \frac{3}{2}k_L^2\lambda_D^2\right)$$

The resulting plasmon frequency spectrum is

$$\omega_{B,R} \approx \frac{\omega_L}{2}\left(1 \pm \frac{3}{4}(k_B^2 + k_R^2)\lambda_D^2\right),$$

where the "+" sign refers to the blue shifted plasmon, travelling with a wave vector component in the direction of the pump laser wave, while the "-" sign refers to the red plasmon, for which $\bar{k}_L \cdot \bar{k}_R$ can be either positive or negative.

3.4. Filamentation

Filamentation and self-focusing. Intense laser radiation propagating into a plasma enhances the intensity modulations initially present on the beam or density unhomogeneities. Where the electromagnetic energy density is higher, due to the ponderomotive forces or to the thermal pressure, the electron density is reduced; this in turn produces, via refractive index effects, a further enhancement of the laser intensity modulations. The process involving only a small part of the laser beam is usually called "filamentation", while "self-focusing" describes the mechanism involving the large scale intensity profile of the laser beam as a whole.

3.5. Resonance absorption.

Laser radiation obliquely incident on a plasma can excite resonant plasma oscillations, at critical density surface, if $\bar{E}_L \cdot \bar{\nabla} n_e \neq 0$. The damping of the excited electron waves transfers the electromagnetic laser energy into the thermal plasma energy.

The classical turning-point for the light wave, impinging on plasma density gradient at an incident angle θ, occurs at density

$$n_e(\theta) = n_c \cos^2(\theta).$$

So, the electric component of laser radiation parallel to the density gradient have to tunnel in the critical surface region to resonant drive electron plasma waves. As a consequence, there is an optimal incidence angle, that maximises such an absorption. In fact, for $\theta \to \pi/2$ the electromagnetic wave have to tunnel too far and the electron plasma wave is not driven efficiently. For $\theta \to 0$ the component of laser electric field parallel to the density gradient vanishes and once again the electron wave is not driven efficiently. The resonance absorption maximises at about 60%, for $sin(\theta) \approx 0.8(\omega_L L / c)^{-1/3}$.

There is a simple way to evidence the dependence of the resonance absorption on laser polarisation and the position of the turning point. The Poisson equation in a plasma

$$\bar{\nabla} \cdot (\varepsilon \bar{E}) = 0,$$

where

$$\varepsilon = 1 - \left(\frac{\omega_p}{\omega_L}\right)^2 = 1 - \frac{n_e}{n_c}$$

is the plasma dielectric constant, can be rewritten in the form

$$\bar{\nabla} \cdot \bar{E} = -\frac{\bar{\nabla}\varepsilon \cdot \bar{E}}{\varepsilon} = \frac{\bar{\nabla} n_e \cdot \bar{E}}{n_c - n_e}.$$

On the other hand

$$\bar{\nabla} \cdot \bar{E} = -4\pi e \delta n_e,$$

where δn_e is the electron density perturbation of the plasma wave. So, equating the right member of the two equations, we obtain

$$\delta n_e = \frac{\bar{\nabla} n_e \cdot \bar{E}}{4\pi e(n_e - n_c)}.$$

The last equation shows that "s" polarised laser radiation, for which $\bar{\nabla} n_e \cdot \bar{E} = 0$, can not drive Langmuir waves, while for "p" polarised radiation, for which $\bar{\nabla} n_e \cdot \bar{E} \neq 0$, the electron density perturbation of the plasma wave increases when the critical density is approached (L. Gizzi et al. 1996).

3.6. Brunel effect.

Very intense laser radiation, obliquely impinging on a metallic surface or a sharply bounded overdense plasma, pulls electrons into the vacuum and sends back them into the plasma with a velocity $v \approx v_E = \frac{eE_L}{m\omega_L}$. Since the electric field is null inside the plasma, one can see that a large part of the kinetic energy, acquired by the electrons in the vacuum, is lost when the electrons reenter the plasma (Brunel F., 1987). This mechanism is more efficient than usual resonant absorption for $v_E/\omega > L$, L being the density scale length. Being proportional to v_E/c, Brunel effect becomes very important at relativistic laser intensities.

3.7. Surface Plasma Waves (SPW).

A sharp plasma boundary, as that created by ultrashort pulses, can support surface waves (Dragila R., 1991). These fluctuations of the electronic density are accompanied by a mixed transversal and longitudinal electromagnetic field. In the case of a SPW propagating on a plasma surface (z=0) in the x direction, the electric field is given by

$$\vec{E}_i = \left(E_{x,i}, 0, \pm E_{z,i}\right)\exp\left[i\left(k_{x,i}x \pm k_{z,i}z - \omega t\right)\right], \quad i = 1,2$$

where the "+" is for z>0 (i=2), while the "-" is for z<0 (i=1). In the physical conditions in which the SPW can be supported, k_x is represented by a complex number; while k_z, which is imaginary, causes the exponential decay of the field, for increasing values of $|z|$.

Due to the dispersion relations of the SPW and of electromagnetic waves, p-polarised laser radiation, impinging on the plasma at an angle θ, can not excite SPW at the vacuum-plasma boundary. To make it possible a low density plasma have to be present in front of the high density plasma boundary, or an electron density modulation at the plasma surface, whose wave number (Δk_x) allows to fulfil the matching conditions

$$k_x = \frac{\omega_L}{c}\sin(\theta) \pm \Delta k_x = k_{SPW} .$$

The damping of the SPW, excited by intense laser radiation, produces a quite efficient absorption of this last in the plasma. In fact, the component of the electric field perpendicular to the plasma surface causes a strong coupling with the resonant absorption.

3.8. Hot electrons.

There are several experimental evidences (based on the measurements of the X-ray spectrum, from laser produced plasmas) of the generation of an electron distribution with two characteristic temperatures. That is, beside an electron population distributed as a Maxwellian at the mean plasma temperature T_c, coexists a strongly minority population ($\frac{n_h}{n_c} \approx 0.01$) distributed as a Maxwellian at a higher temperature T_h (S. Bastiani et al. 1995), (L. Gizzi et al. 1996).

These hot electrons are produced by different causes.

A first cause is represented by the several mechanisms that inhibit the electron thermal conduction (Spitzer L., 1962; Malone R.C., 1975; Manhreimer W.M., 1974), from the critical surface towards high-density plasma regions. In this case a narrow under critical region, just behind the critical surface, reaches very high temperature, and the production of hot electrons and ions becomes possible. Taking into account the inhibited electron thermal conduction, one gets, for the hot electron temperature, $T_h \propto \left(I\lambda^2\right)^{\frac{2}{3}}$.

Another cause is the resonant absorption, which produces at the critical surface a strongly peaked and intense electric field, parallel to the plasma density gradients (Kruer L., 1988). Numerical simulations (Deneef C.P., 1977) has been performed to study the effect of these electric fields on electron distribution. It has been found that slow electrons, covering a small fraction of this high field region during a period, suffer an oscillating electric field, which do not produces valuable increase of their kinetic energy. On the other hand, the very fast electrons cross that region in a very small fraction of period, so suffering a constant electric field. However, due to the short duration of the electric field action, the electron energy variation keeps very small. On the contrary, electrons with an intermediate speed, crossing the region in a fraction of period ($\Delta t \le \frac{1}{2}T$), can gain as much energy as their initial kinetic energy. In this case the hot electron temperature scales as $T_h \propto \left(I\lambda^2\right)^{\frac{1}{3}}$ (Kruer W.L, 1977; Forslund, 1977).

Finally, the electrons can be accelerated up to supra thermal energies by the electric field of the intense laser radiation or by that of the plasma waves. In the case of the transversal electromagnetic wave, the maximum electron energy gain is

$$\Delta\varepsilon_{max} = \frac{1}{2}mv_F^2 \frac{1}{\left(1 - \frac{v_x}{v_\phi}\right)^2}$$

where v_x is the component of the electron velocity along the propagation direction of the wave, whose phase velocity is v_ϕ. Because the phase velocity of a electromagnetic wave propagating in a plasma is larger than the speed of the light in the vacuum,

$$v_\phi = \frac{c}{\sqrt{1 - \frac{\omega_P^2}{\omega_L^2}}} > c,$$

the electron remains only for a short time under the action of an electric field of the same sign. So, the simple interaction between electrons and an electromagnetic plane wave do not produces fast electrons, unless for very high laser intensities. In the case of interest, i.e. for electrons with a low initial speed $\frac{v_x}{v_\phi} \ll 1$, we find, for $\lambda = 1\mu m$ and $I = 10^{15} W/cm^2$, $\Delta\varepsilon_{max} \approx 200eV$; but, for a relativistic intensity $I = 10^{19} W/cm^2$, one gets $\Delta\varepsilon_{max} \approx 0.5MeV$.

In the case of a longitudinal electron plasma wave, the phase velocity can be relatively low

$$v_\phi = v_e\left[3 + \frac{1}{(k\lambda_D)^2}\right]^{\frac{1}{2}},$$

so that some electrons can stay long time in a region of constant sign electric fields and gain much energy from the wave. In the optimal condition the electron energy gain is

$$\Delta\varepsilon_{max} = 4mv_\phi^2\left(\frac{v_E}{v_\phi}\right)^{\frac{1}{2}},$$

where v_E is the electron quiver velocity, due to the electric field of the plasma wave. The amplitude of the electric field of the plasma wave can be obtained by the Poisson equation: $E = \frac{4\pi\delta n_e e}{k}$. If we introduce the ratio between the phase and the thermal velocity $\eta = \frac{v_\phi}{v_e}$, and approximate the ratio of the quiver velocity to the phase velocity

$$\frac{v_E}{v_\phi} = \frac{eEk}{m\omega^2} = \frac{\delta n_e}{n_e}\left(\frac{\omega_p}{\omega}\right)^2 \approx \frac{\delta n_e}{n_e},$$

we can rewrite the previous formula for the energy gain as follows

$$\Delta\varepsilon_{max} = \frac{1}{2}mv_e^2 8\eta^2\left(\frac{\delta n_e}{n_e}\right)^{\frac{1}{2}}.$$

If we consider, as reasonable values, $\eta = 10$, $\frac{\delta n_e}{n_e} = 0.1$, T_e=0.5keV, we obtain $8\eta^2\left(\frac{\delta n_e}{n_e}\right)^{\frac{1}{2}} \approx 250$ and $\Delta\varepsilon_{max} = 125keV$.

4. X-ray emission from laser produced plasmas.

The thermal energy acquired by the plasma electrons in the laser absorption processes is mainly dissipated by three radiative mechanisms. In the first, the free electrons, interacting with the Coulomb potential of the ions, radiate in a continuum electromagnetic spectrum. In the second, free electrons, captured by ions, radiate in a continuum electromagnetic spectrum, corresponding to the transitions from the initial free electron state to the one of the bound electron. The third emission mechanism produces a line spectrum, corresponding to the electron transitions between discrete levels of the ionised atoms.

4.1. Bremsstrahlung.

Let consider an electron, with an initial velocity v, interacting with an ion, with an impact parameter b. The interaction characteristic time is $\tau \approx \frac{2b}{v}$. So, the dominant frequency in the radiated electromagnetic spectrum is $\nu \approx \frac{1}{2\pi\tau} = \frac{v}{4\pi b}$.

On the other hand, the energy radiated (ΔE) during a single electron-ion impact can be evaluated on the basis of the maximum acceleration suffered by the electron ($a = \frac{Ze^2}{b^2 m}$):

$$\Delta E = \frac{2e^2a^2\tau}{3c^3} \approx \frac{2}{3}\frac{Z^2e^6}{m^2c^3b^3v}.$$

The number of collisions with ions that an electron undergoes in unit time, with an impact parameter ranging from b to b + db, is $2\pi n_i v b\, db$. So, the power radiated per electron is:

$$w = \int \Delta E 2\pi n_i v b \cdot db \approx \frac{2}{3}\frac{Z^2e^6}{m^2c^3} 2\pi n_i \int_{b_{min}}^{b_{max}} \frac{db}{b^2},$$

where $b_{max} \approx \lambda_D$, while b_{min}, being determined by the uncertainty principle, came to be just the De Broglie wavelength $b_{min} \approx \frac{h}{2\pi mv}$. Being $b_{min} << b_{max}$, the integration gives:

$$w \approx \frac{8\pi^2}{3}\frac{e^6}{mc^3h} Z^2 n_i v.$$

Considering a Maxwellian distribution of electron velocities:

$$f_e = n_e\left(\frac{m}{2\pi k_B T_e}\right)^{\frac{3}{2}} \exp\left(-\frac{mv^2}{2k_B T_e}\right),$$

we can obtain the Bremsstrahlung power radiated per unit volume (W_B), by performing the integral:

$$W_B = \int_0^\infty w \cdot f_e \cdot 4\pi v^2 dv.$$

Due to the approximations in the previous calculations, we have to multiply the final result by $2/3^{1/2}$, to obtain the correct numerical result:

$$W_B = \frac{32\pi^2}{3^{\frac{3}{2}}} \frac{Z^2 e^6}{mc^3} \frac{n_e n_i}{h} \left(\frac{2k_B T_e}{\pi m}\right)^{\frac{1}{2}} = 1.6 \cdot 10^{-27} Z n_e^2 T_e^{\frac{1}{2}} erg\,\sec^{-1} cm^{-3}.$$

The characteristic dependence of the Bremsstrahlung emission on electron density and temperature is apparent.

To evaluate the spectral Bremsstrahlung emission, we have to start from the relation between the frequency and the impact parameter and perform the previous integral, integrating on ν instead of b:

$$w = \int \Delta E 2\pi n_i v b \cdot db = \frac{2}{3} \frac{Z^2 e^6}{m^2 c^3} 2\pi n_i \int_{b_{min}}^{b_{max}} \frac{db}{b^2} = -\frac{2}{3} \frac{Z^2 e^6}{m^2 c^3} \frac{8\pi^2 n_i}{v} \int_{\nu_{min}}^{\nu_{max}} d\nu = A \int_{\nu_{min}}^{\nu_{max}} d\nu = A \nu_{max},$$

where $\nu_{max} = \frac{mv^2}{2h}$, $\nu_{min} = \frac{\nu}{4\pi\lambda_D}$ and the final result has been obtained considering that $\nu_{max} >> \nu_{min} = 0$. As we can see, the energy radiated by an electron of velocity v per unit frequency, in the frequency range $0 < \nu < \nu_{max}$, is a constant (A) in inverse proportion to ν,and is zero for $\nu > \nu_{max}$. So, the contribution to the frequency ν comes only by those electrons, whose velocity is $v > \left(\frac{2h\nu}{m}\right)^{\frac{1}{2}}$. Performing the integration to take into account the contribution of the whole electrons of the Maxwellian distribution and correcting by the factor $2/3^{1/2}$, we obtain the spectral intensity:

$$W_B^\nu = \frac{2}{3^{\frac{1}{2}}} \int_{\left(\frac{2h\nu}{m}\right)^{\frac{1}{2}}}^{\infty} A \cdot f_e \cdot 4\pi v^2 dv = \frac{32\pi}{3} \left(\frac{2\pi}{3k_B T_e m}\right)^{\frac{1}{2}} \frac{Ze^6 n_e^2}{mc^3} \exp\left(-\frac{h\nu}{k_B T_e}\right) \approx$$

$$6.8 \cdot 10^{-38} Z n_e^2 T_e^{-\frac{1}{2}} \exp\left(-\frac{h\nu}{k_B T_e}\right) erg\,\sec^{-1} cm^{-3} Hz^{-1}$$

Taking into account the relation between the spectral intensity per unit of frequency and that per unit of wavelength, we also obtain the useful expression:

$$W_B^\lambda = W_B^\nu \frac{c}{\lambda^2} d\lambda \approx 2 \cdot 10^{-27} Z n_e^2 T_e^{-\frac{1}{2}} \lambda^{-2} \exp\left(-\frac{h\nu}{k_B T_e}\right) erg\sec^{-1} cm^{-4}.$$

The maximum of the spectral emission is for $\frac{hc}{\lambda k_B T_e} \approx 2$, to which corresponds $\lambda \approx \frac{0.72}{T_e^{\frac{1}{2}}} cm$.

This bell shaped distribution is similar to that of black body

$$u_\lambda = \frac{8\pi hc}{\lambda^5} \left[\exp\left(\frac{hc}{\lambda k_B T}\right) - 1\right]^{-1} erg cm^{-4},$$

whose spectral energy density is however peaked, for the same temperature, at shorter wavelength. In fact the maximum of the spectral distribution of the energy radiated by the black body is for $\frac{hc}{\lambda k_B T_e} \approx 5$, to which corresponds $\lambda \approx \frac{0.29}{T_e^{\frac{1}{2}}} cm$. Moreover the black body emission, spectrally integrated, scales as T^4 (Stefan law), while that of the Bremsstrahlung as $T^{1/2}$.

4.2. Recombination.

When a free electron is captured by a (Z+1)-fold ionised atom, carrying out a transition to a bound state of a Z-fold ionised atom, a photon is emitted, whose energy is

$$h\nu = \frac{1}{2} mv^2 + E_Z^n$$

where the first term, in the right side of the equation, represents the kinetic electron energy and the second the bound energy of the final atomic state; Z is the ion charge and n the principal quantum number. Due to the continuum values of the initial electron energies, the radiation is emitted in a continuum frequency spectrum. However the contribution of each transition to the continuum is for $h\nu \geq E_Z^n$ (recombination edge), so that the continuum recombination spectrum is characterised by "jumps", corresponding to the different recombination edges.

The spectral intensity of the recombination continuum can be expressed in terms of that of Bremsstrahlung

$$W_r^\nu = W_B^\nu 2 \frac{Z^2 E_H}{k_B T_e} \sum_1^\infty \frac{1}{n^3} \exp\left(\frac{Z^2 E_H}{n^2 k_B T_e}\right) =$$

$$2.2 \cdot 10^{-32} Z^3 n_e^2 T_e^{-\frac{3}{2}} \sum_1^\infty \frac{1}{n^3} \exp\left(\frac{Z^2 E_H}{n^2 k_B T_e} - \frac{h\nu}{k_B T_e}\right) erg\,\sec^{-1} cm^{-3} Hz^{-1}$$

where E_H=13.6eV is the Hydrogen ionisation energy, and, for what said before, the argument of the exponential keeps always negative.

Similarly for the ratio of the spectrally integrated recombination and Bremsstrahlung intensities we have

$$\frac{W_r}{W_B}=\frac{\int_{\frac{Z^2E_H}{n^2h}}^{\infty}W_r^{\nu}d\nu}{\int_0^{\infty}W_B^{\nu}d\nu}=\frac{2Z^2E_H}{k_BT_e}\sum_{n=1}^{\infty}\left[\frac{1}{n^3}\exp\left(\frac{Z^2E_H}{n^2k_BT_e}\right)\right]\frac{\int_{\frac{Z^2E_H}{n^2h}}^{\infty}\exp\left(-\frac{h\nu}{k_BT_e}\right)d\nu}{\int_0^{\infty}\exp\left(-\frac{h\nu}{k_BT_e}\right)d\nu}=$$

$$\frac{2Z^2E_H}{k_BT_e}\sum_{n=1}^{\infty}\frac{1}{n^3}\approx 2.4\frac{Z^2E_H}{k_BT_e}$$

As we can see, the Bremsstrahlung overcomes the recombination emission for low Z, high temperature plasmas.

4.3. Lines.

In a plasma, beside free electrons and completely stripped nuclei, atoms and ions are present. So transitions of bound electrons from excited to lower states can still contribute to the radiated energy. The major contribution to this spectral discrete emission is from the transition to the ground state (resonance lines). However, transitions between excited states, even if weaker, are usually more interesting for diagnostic purposes, because they are generally less reabsorbed in the plasma.

Let us consider the emission coefficient (specific power per unit volume, steradiant and frequency interval) corresponding to the transition from the state 2 to the state 1

$$\varepsilon_{\nu}=\left(\frac{h\nu}{4\pi}\right)A_{2,1}n_2L(\nu-\nu_{2,1})\frac{erg}{cm^3\cdot sec\cdot Hz\cdot strad}.$$

where

$$A_{2,1}=\frac{8\pi h\nu^3}{c^3}B_{2,1}=\frac{64\pi^4}{c^3h}\nu^3P_{2,1}^2\,sec^{-1}$$

is the spontaneous emission coefficient, n_2 the number density of ions in the upper state 2, $L(\nu-\nu_{2,1})$ the line shape function and $\nu_{2,1}$ the central frequency of the transition between the two state of energy E_1 and E_2. $A_{2,1}$ and $B_{2,1}$ represent respectively the probability per unit time of spontaneous and induced emission; $P_{2,1}^2$ being the modulus square of the matrix element of the electric dipole moment evaluated between the two state. The line shape function $L(\nu-\nu_{2,1})$, describing the emitted spectrum close to the central frequency $\nu_{2,1}$, is a normalised function of the frequency:

$$\int_0^{\infty}L(\nu-\nu_{2,1})d\nu=1.$$

The level energies and the A-values are considered as intrinsic properties of the radiating ions or atoms and the tabulated values (Martin, 1980) are obtained by quantum mechanics calculations and more or less indirect measurements. On the other hand, the level populations and the line shapes depend on the physical parameters of the plasma, in which the radiating atoms or ions are imbedded. In particular, the populations are determined by the dynamical balance of several collisional and radiative processes inside the plasma.

Three are the main physical processes that determine the line shape: 1) the thermal motion of the radiating atomic systems (Doppler broadening); 2) the finite radiative lifetime of the bound states involved in the transition (natural broadening); 3) the interaction of the radiating systems with the rest of the plasma (pressure broadening).

1) In the non-relativistic limit, the Dpppler shift

$$\Delta\nu=\frac{v_x\nu}{c}$$

is proportional to the velocity component in the line of sight. So, for a Maxwellian distribution of the electron velocities, we have

$$L(\nu-\nu_{2,1})=L_0\exp[-\left(\frac{2\sqrt{\ln 2}(\nu-\nu_{2,1})}{\Delta\nu_D}\right)^2],$$

where

$$\Delta\nu_D=\frac{2\nu_{2,1}}{c}\sqrt{\frac{2\ln 2k_BT_e}{M}}\approx 7.16\cdot 10^{-7}\sqrt{\frac{T_e}{A}},$$

is the FWHM (full width at half maximum intensity) of the spectral line, A being the atomic mass number and T_e being expressed in Kelvin.

2) The natural line broadening is determined by the sum of transition probabilities for all spontaneous transitions originating from both upper and lower levels of the considered line. In this case the line shape is a Lorentzian

$$L(\nu-\nu_{2,1})=\frac{L_0}{1+\left[\frac{2(\nu-\nu_{2,1})}{\Delta\nu_N}\right]^2},$$

where

$$\Delta\nu_N=\frac{1}{2\pi\tau_1}+\frac{1}{2\pi\tau_2},$$

t_1 and t_2 being the mean life of the two levels.

3) The pressure broadening is due to the interactions of the radiating systems with the other particles of the plasma. If σ represents the cross section for the considered interaction, the FWHM of the line shape, that still appears more or less Lorentzian, is

$$\Delta\nu_p\approx\frac{1}{2\pi\tau_p}\approx\frac{\sigma v_{rel}n_p}{2\pi},$$

where n_p is the number density of the perturbers and v_{rel} the relative velocity of the interacting atomic systems.

The Stark broadening is the most important subclass in the context of the pressure broadening mechanisms. This broadening is due to the interaction of the radiating system with the microscopic electric field produced from the rest of the plasma on it.

Usually, in plasmas the natural line width is negligible compared with the Doppler and Stark width; this last being more important at high plasma densities and for hydrogen-like ions. However, the observed line widths are very often due to experimental conditions such as the instrumental spectral resolution or the dimension of the emitting plasma source.

4.4 Radiation transport in plasmas.

As a general rule, a medium can absorb the frequencies that it radiates. In condition of thermal equilibrium, this is expressed by the Kirchhoff law that connects the emitting power of a body (the power radiated per unit surface, steradiant and frequency) and its spectral absorptivity (the ratio of the absorbed monochromatic power to that impinging on the surface) to the emitting power of the Black-Body, that is an universal function of temperature and frequency:

$$e(\nu,T) = \alpha(\nu,T)\cdot e^{BB}(\nu,T).$$

The hemispherical emitting power of the Black-Body is related to its energy density $u^{BB}(\nu,T)$, by the simple relation:

$$e^{BB}(\nu,T) = \frac{c}{4}u^{BB}(\nu,T) = \frac{c}{4}\frac{8\pi h\nu^3}{c^3}\left[\exp\left(\frac{h\nu}{k_BT}\right)-1\right]^{-1}.$$

The radiation emitted by a plasma element of thickness dx per steradiant is

$$dI = \varepsilon\cdot dx - Ik\cdot dx,$$

where ε is the emission coefficient (due to ff, fb, bb emission) and k is the effective absorption coefficient. The equation states that the intensity of radiation increases (due to the emission processes) of εdx and decreases (due to the absorption mechanisms) of $Ikdx$ while it propagates in the plasma on a distance dx.

The pervious equation can be rewritten in the following form

$$\frac{dI}{d\tau} = \frac{\varepsilon}{k} - I = S - I,$$

where $d\tau = kdx$ and S is the source function, that in the case of thermodynamic equilibrium is related to the Planck function as follows:

$$S = \frac{\varepsilon}{k} = \frac{c}{4\pi}u^{BB}(\nu,T).$$

The adimensional quantity τ is the optical depth

$$\tau = \int_0^x k\cdot dx,$$

which take into account the opacity effects suffered by the radiation propagating in the plasma.

The integration of the radiative transport equation is not straightforward, because ε and k depend on time and the space coordinates in the plasma. Therefore, let us consider the case of a stationary, homogeneous plasma, in which case, by integrating the equation we obtain:

$$I(\tau) = I(0)\exp(-\tau) + \frac{\varepsilon}{k}[1-\exp(-\tau)],$$

where I(0) is a source term at x=0, that vanishes if we consider the pure plasma self-emission.

Two relevant physical conditions have to be considered. The first, $\tau<<1$, corresponds to that of optically thin plasma.

$$I(\tau) \approx \varepsilon\cdot x,$$

The intensity of the radiation outgoing from the plasma is proportional to the plasma thickness and to the emission coefficient related to the different emission mechanisms (ff, fb, bb) activated inside the plasma.

The second, $\tau>>1$, corresponds to the condition of optically thick plasma. In this case the radiated intensity is independent on the plasma thickness and the strong radiation auto absorption deeply modify the original spectrum of the energy radiated by the plasma interior. In the thermal equilibrium conditions, the spectral distribution of the radiated intensity approaches that of Black-Body:

$$I(x) \approx \frac{\varepsilon}{k} \approx \frac{c}{4\pi}u^{BB}(\nu,T).$$

From the previous considerations follows that auto absorption effects in plasma radiation have to be considered whenever $\tau\approx 1$. Moreover, a plasma can be considered optically thick for some frequency range and thin for another range. For the same reason auto absorption effects start to came important for the frequencies about the line shape maximum and successively for those of the line tails.

4.7. Characteristics of laser-plasma X-ray sources.

A laser-plasma X-ray source is generated by focusing a high power laser pulse onto the surface of a target which is held in vacuum. The used laser parameters range considerably: pulse durations from 50fs to 50ns; energies from 1mJ to 10 KJ; laser intensities from 10^{10} to 10^{20} W/cm^2. For each incident laser pulse an X-ray pulse is emitted, into the $\approx 2\pi$ solid angle in front of the target, whose duration is roughly the same as the impinging laser pulse. After the generation of every laser-plasma X-ray pulse a crater is produced on the target surface, so that a new piece of the target surface has to be used for the next shot. Quasi-CW X-ray sources are produced by focusing low energy, high repetition rate pulsed lasers onto rotating cilindrical target to provide a fresh target surface for every shot.

The leading edge of the focused laser pulse vaporises and ionises the matter at the target surface layer. A low temperature expanding plasma is created, which strongly absorbs the remainder of the laser pulse, so that the plasma temperature rises to ≈0.1-1KeV. The heat, transported trough the plasma, vaporises more target material. This new produced plasma replenishes that lost from the focused laser beam waist due to the hydrodynamic expansion. On a time scale of ≈100ps a stady state plasma flow is established, which lasts until the end of the laser pulse. The main X-ray yield is caming from the plasma region which combines both high temperature and high electron density. The dimensions of this region as well as that of the produced crater are of the order of 100μm.

4.7.1. Spectral distribution.

As a crude approximation, we can consider the spectrum of the electromagnetic radiation emitted by a laser produced plasma like that of a black body at the same temperature. So, for tipical temperatures of hundreds of eV, a very wide spectrum is emitted, ranging from the infrared to the X-ray region.

However, loocking in more details to the two emissions, several and relevant differences become apparent. First of all the black body is a physical system at thermal equilibrium, radiating in a pure continuum spectrum; while the majority of the plasmas of interest are systems far from the thermodinamic equilibrium, radiating in a continuum as well as a discrete spectrum. Moreover, considering the only continuum emission component, we observe that, for a same temperature, the maxima of the plasma and black body spectral distributions do not overlap. In the case in which the plasma continuum emission is dominated by the Bremsstrahlung mecanisms, the plasma spectral distribution peaks at a wavelengths ≈2.5 times longer than for the black body spectral distribution.

The other contribution to the continuum emission is represented by the electron recombination into bound states. This mechanisms gives to the continuum a contribution progressively decreasing with the photon energy, starting from the different ionization energies. As a result, the recombination produces characteristics "jumps" in the continuum spectrum, sed "recombination wedge".

The discrete component in the plasma electromagnetic emission is due to electron transitions between two bound states (resonance lines). However, a second kind of line emission results from duobly excited states of ions. These lines are less intense than the resonance lines of the ion, and occur at slightly longer wavelength.

When target material of high atomic number (Z) are used, recombination continuum as well as line radiation carry most of the radiated energy. As an example, in the case of Aluminium target irradiated by 3ns pulses of the Nd:Glass laser third harmonics (0,35μm) at intensities of 10^{14}W/cm^2, the 30% of the radiated energy is in lines, the 60% in recombination continuum and the 10% in Bremsstrahlung (Duston D., 1985).

Acting on the atomic number (Z) it is possible to control the spectral characteristics of the laser-plasma X-ray source.

By using very low Z targets (plastics) a plasma is produced in which the most abundant ionic species is that of completely stipped atoms. The radiation emitted by such a kind of plasmas is almost free from line emission, and the continuum is due to the Bremsstrahlung mechanisms.

For higher Z values, but with Z≲20, the produced plasma is predominantly populated by ionic species where all but the last one or two electrons have been removed from the atoms. In these conditions a single line can carry a significant fraction (a few %) of the plasma X-ray emission, in the photon energy range from 0.5 to 10KeV. Due to the sharpness of the line emission ($\Delta\nu/\nu \approx 100$), the line intensity can overcome the continuum emission intensity (for considered Z values, the recombination overcomes the Bremsstrahlung) for several order of magnitude. These X-ray sources are fruitfully used in spectroscopic applications, where bright line-emitters are required.

When high Z targets (Z≳20) are used, the plasma is populated by ions with several bound electrons. The resulting spectrum of

the radiated energy is dominated by a very complicated many-electron line emission. The great line density in the spectrum produces a complete overlap giving an effective, continuous band emission, which can not be spectrally resolved even if examined by using high resolution spectrograph. We can see that targets with very low Z values, as well as with high Z values produce continuum X-ray emission. However the conversion efficiency of laser to X-ray radiation increases with Z. So, high Z targets are preferred as band emitters, when background sources for absorption spectroscopy are required.

4.7.2. X-ray pulse duration.

As a general rule, the X-ray pulse duration is coparable to that of the laser pulse producing the plasma. It depends on the characteristic times needed to heating the plasma and to cooling down by radiation and free expansion. These times are of the order of tens of ps. So, when a plasma is generated by using laser pulses ≈1ps duration, X-ray pulses of up to 20 ps duration at photon energy hν ≈100eV are produced (Landen O.L., 1987).

The time duration of the X-ray emission strongly depends on the considered spectral range. Keeping constant all the remaining physical conditions, more energetic is the detection spectral range, shorter results the time duration of the X-ray emission. In fact X-rays of higher frequency ranges are produced for higher plasma temperatures, which are maintained for a shorter time, after the end of the laser pulse. Let consider, for example two experiment in which 25ns KkF laser pulses were used. In the first experiment (Tooman T.P., 1986)the detection spectral range was at 15eV≤hν≤73eV and the laser pulses were focused on an Au target at an intensity of $10^{12}W/cm^2$. In this case the half-width of the X-ray pulse was ≈40ns, which is nearly a factor two longer than the laser pulse. In the second experiment (Davis G.M., 1988) the detection spectral range was at hν≈1KeV and the laser pulses were focused on a Cu target at an intensity of $10^{14}W/cm^2$. In this case the half-width of the X-ray pulse is only ≈5ns, which is much shorter than the laser pulse duration.

4.7.3. Source size, and emission angular distribution.

Usually the laser beam is focused at a small angle with respect to the target surface normal, to avoid dangerous reflections, which could damage the oscillator and the first amplification stages of the laser system. Nevertheless, the plasma plume that develops shows a cylindrycal symmetry, whose axis is orthogonal to the target surface.

As long as the laser pulse duration keeps shorter than the characteristic times of the plasma hydrodynamic expansion, the source size is determined by that of the laser focal spot. In these conditions the plasma emitting volume can be very small: almost a point source radiation, a few micrometers wide.

For laser pulse duration still shorter, but comparable with those of the hydrodynamic expansion, the X-ray source shows a cylindrical shape, whose diameter is of the order of the focal spot size, while the heigth is given roughly by the product $v_s\tau$, where v_s is the sound velocity in the plasma and τ is the laser pulse duration. For even more longer laser pulse duration, the X-ray source shows the typical cigar shape, whose longitudinal and transversal dimensions depend on the heat transport and matter ablation mechanisms.

The apparent source size strongly depends on the spectral window of the imaging system (for istance the filter in front of the pin-hole camera). In fact harder are the detected X-rays, saller is the plasma region at higher temperature in which that radiation can be generated.

Also the angular distribution of the X-ray emission from the laser produced plasma shows a cylindrical simmetry, whose axis is orthogonal to the target surface, independly on the incidence angle of the laser beam. Experimentally has been found that the angular distribution of laser-plasma emission fits the function

$$I_\lambda(\theta) = I^*_\lambda(\cos(\theta))^n,$$

where θ is the angle, respect to the surface normal, at which X-rays, of wavelength λ, are detected, and n is a parameter that ranges in different experimental conditions, from ≈0.3 to ≈3.

4.7.4. X-ray conversion efficiency.

The X-ray conversion efficiency depends on the target atomic number (Z) and the laser parameters.

Keeping constant all the laser-plasma interaction parameters, but the target atomic number, has been obseved that the X-ray conversion efficiency shows four maxima as the atomic number of the target is progressively increased from Z=4 (beryllium) through to Z=92 (uranium) (Glibert K.M., 1980). The physical reason of this characteristic behaviour is that, as the Z of the target increases, the line emissions produced by the electron transition to some final shell (K, L, M, N,...) give successively their own contribution. The location of these maxima is a function of the spectral range being observed (Mochizuki T., 1987). In fact, the

spectral range, concerning some shell emission (for example L-shell emission), depends on the atomic number of the target.

Therefore it is possible to "tune" the X-ray emission from the laser-produced plasma, by choising the atomic number of the target. However the laser intensity have to be high enough to reach a plasma temperature suitable to excite the ion species of interest for the considered shell emission.

Several experiment have been performed to investigate on the dependence of the X-ray conversion efficiency on the laser wavelength. The shorter wavelengths were found to couple more favourably into the target plasma, due to the higher absorption and the smaller fraction of the absorbed energy lost to excite fast electrons. In fact the shorter wavelengths can penetrate in denser plasma regions, where the collisional absorption is more efficient, as well as the collisional excitation of ions giving higher X-ray emission. The first, clear demonstration of the advantages of using short wavelengths to generate X-ray radiation from laser produced plasma was the Yaakobi experiment (Yaakobi B., 1981). In that experiment the X-ray conversion efficiency of the fundamental (λ=1.06μm) and 3rd harmonic (λ=0.35μm) of a Nd laser was compared. The conversion efficiency of the UV laser radiation was found to be ten times higher than of the IR laser.

The other laser parameter influencing the X-ray conversion efficiency is the laser intensity. In fact the laser intensity determines the plasma temperature ($T \propto I^{0.5}$), which in turn determines the plasma degree of ionization and the efficiency of excitation of the different ionic species. The behaviour of the efficiency versus laser intensity, strongly depends on the detection spectral window. For instance if the window fits the spectral range of some shell emission, the efficiency shows a typical threshold-type behaviour, because there is a suddenly increase for the laser intensities that allow to the shell transitions to be accomplished. The efficiency remains almost constant for a further increase in the laser intensity, but it start to decrease when intensities are reached as high as to allow to produce electron transition to the more inner shell (Charker M., 1986; Batani D, 1993).

Finally we observe that the laser focusing conditions on target have to be accurately controlled in order to maximize the X-ray conversion efficiency. It is well known that the intensity of X-ray emission from laser-produced plasmas strongly depends upon the laser focusing configuration on target (Amiranoff F., 1979; Tallents G.J.,1986). The X-ray flux have to be maximized by scanning the target position along the beam axis, in the proximity of the nominal focal position. In a ns laser pulse regime experiment (Bastiani S., 1995; Macchi A., 1996) the maximum of the X-ray conversion efficiency was found with the target displaced 0.5mm with respect to the position of the beam waist, in the direction of the propagation of the laser ligth. In the position of maximum X-ray emission the X-ray yield is characterized by a large variability shot by shot. This feature can be explained taking into account the effect of filamentation process on local plasma conditions. In fact, when the target is in the optimum position, the laser beam waist lies in the plasma blow-off. In this particular configuration, the plasma can further contribute to focus the laser light due to the filamentation instability, thus enancing the X-ray emission. The X-ray signal variability would be, in this case, a consequence of the non linear character of the filamentation instability. A further confirmation of this interpretation is represented by the quite different dependence of the X-ray yield on laser intensity, for the target in the position of maximum X-ray emission and in another (marginal) position (Bastiani S., 1995). In the first case, experimental data points are fitted by a curve more than quadratic, in the second case by a straight line. Also, in the first case the experimental data points are more scattered than in the second case, thus supporting the conclusions that the laser-plasma interaction process is influenced by a non linear interaction mechanism. It is interesting to observe that measurements of second harmonic emission intensity versus target position and laser intensity, performed in similar experimental conditions (Biancalana V., 1993) showed a similar behaviour.

4.8. High harmonics generation in plasmas.

A promising approach for generating coherent, monocromatic radiation in the soft X-ray region is through high harmonic generation. In recent experiments, by focusing ultrashort visible laser pulse ($\leq$1psec) at high intensity ($\geq 10^{17}$W/cm^2) into a gas target high harmonics (up to $\simeq$100) have been generated, with reasonable efficiency. Typical output energies ($\simeq$10nJ) obtained in this way are low compared to an X-ray laser and too small for many applications. However, this radiation remain interesting for a wide range of scientific investigations.

4.9. X-ray lasers.

Short wavelengths lasers offer significant technological reward in several research applications, where coherent radiation is required, as the holography and the interferometry on sub-micrometer scale. Despite the relevant international effort

directed towards the development of this kind of sources, only with difficulty X-ray lasing has been achieved in a limited wavelength range (400-35Å). This is due to fundamental physical reasons, inducing severe technological impediment to the development of X-ray lasers.

X-ray lasers require pumping powers as high as 10^9 times the optical lasers. In fact for the first the the energy transitions are of the order of the KeV and the corresponding lifetimes of the order of the picosecond; while for the second the energy are of the order of the eV and the lifetime of the order of microseconds. These enormous pumping powers can not delivered by flashes or other ordinary pumping systems, but only by very high power laser. This is the reason for why research activity on X-ray lasers can be developed only at large laser facilities like Livermore (USA) or RAL (UK).

The matter irradiated at so high power density is in the plasma state and the X-ray lasers operate on valence electron transitions in high stripped ions. The X-ray laser is basically constituted by a large aspect ratio cylinder of small dimensions, whose lasant material is an high density plasma, hard pumped by a short and high power laser pulse. The absence of optical materials, in the conventional sense, for the X-ray wavelengts implies as aconsequence that the laser have to operate in a high gain mode in which the spontaneous emission is amplified in a single pass of the lasant element. This represents a serious limit in the coherence properties of the X-ray laser.

Since the years of their invention the development of the lasers has been marked by the effort of the achievement of the physical conditions for the laser emission at progressively shorter wavelength.

In the middle 1950's the first maser was built-up, generating microwaves with a wavelength of few centimetres. In the 1960's the first optical lasers came to be employed in the laboratories, their operating wavelength being a factor 10^{-5} shorter than that of maser. Afterwards, lasers operating in ultra-violet region have been set-up, till, in the 1980's, the fist x-ray lasers became to operate, at wavelengths 10^{-2} times shorter than the optical lasers.

The numerous applications profit by the coherence and the short wavelength of the X-ray laser radiation. So, holograms of microscopic biological structures, too small to be investigated with visible light, can be created. In this way, for the first time, biologists have visualised the three-dimensional structure of the DNA.

The working principle of an optical as well as an X-ray laser is the same. An intense energy source (flashes or electrical discharge) produces a population inversion on electron levels of the active material. The induced decay mechanism produces, from the so activated material, emission of a very intense radiation, that results strongly monochromatic, directional and coherent.

However simple considerations show as the power needed to pump an X-ray laser largely exceeds that of an optical laser. The energy levels, the transition energy between such levels, as well as the ionisation energies scale, in the simplest atomic model, as Z^2; where Z represents the effective nuclear charge for an outer bound electron. So an active material for an X-ray laser, operating at wavelength 10^{-2} that of an optical laser, have to be constituted by relatively heavy atoms, whose Z is of the order of 10. Consequently, the required pump energy for X-ray laser is 10^3 times that of optical lasers: 10 for the required ionisation and 10^2 for the increased laser level separation.

This energy has to be released in a time 10^4 times shorter than in the case of optical lasers. In fact the rate at which electrons spontaneously decay to lower energy levels scales as Z^4.

In a high power solid state laser the typical pump energy is of the order of 10 KJ, delivered in a time of the order of 1msec. This means that, for an X-ray laser, the required pump power is of the order of 10^{14}W= 10^2TW. This power can be delivered only by the most powerful solid state laser operating in the nsec pulse regime, or by Ti:sapphire lasers, operating in the fsec regime.

The excitation scheme we are describing is referred as collisional excitation. It is carried out by focusing the beam of an high power laser o a thin strip ($1x10^{-2}x10^{-5}$cm) of the suitable laser material, for instance Selenium. The target irradiation produces an high temperature (1KeV) Selenium plasma, whose atoms (32 electrons) are stripped of their outer 24 electrons. The electron-ion collisions induce transition from the ground state $1s^22s^22p^6$ (2p for short) to the higher energy levels like$1s^22s^22p^5$ 3s (3s for short) and $1s^22s^22p^5$ 3p (3p for short). Because the transition from the 3p to the 2p ground state is quantum-mechanically forbidden, while electrons decay very rapidly back to the ground state, a population inversion between the 3p and the 3s levels is produced. In fact in this conditions 96 percent of the ions have electrons in 2p state, 3 percent in 3p state and 1 percent in the 3s state. When transitions from the 3p to the 3s state are spontaneously produced, 200 Å soft X-ray photons are emitted, that initiate the lasing action by stimulating other similarly excited ions to emit photons of the same wavelength.

The amplification of this radiation is problematic, due to the difficulty of producing good multilayer mirrors for soft X-ray radiation. So the majority of X-ray lasers till now are operated in single pass conditions; i.e., in such a way that photons pass through the active medium only once.

The most important evidence of the lasing action is the exponential dependence of the intensity of laser radiation on the length of the cylindrical plasma in which the laser action take place.

Typical values of the X-ray laser power are 10-100 MW, in a pulse lasting ≈100psec.

Numerous X-ray laser pumping schemes have been tested, with the goal of reaching shorter operating wavelengths and higher efficiency. Among them the most popular is the recombination scheme, in which the population inversion is obtained by the recombination of the free electrons in the bound states of the ions. However, the output powers of the X-ray lasers operating by collisional pumping, have not achieved till now by the lasers operating with the other pumping mechanisms.

4.10. X-ray emission in ultra-short pulse interactions

The duration of X-ray pulses, along with the spectral properties and the intensity, is a key parameter in view of applications to radiography of rapidly evolving phenomena. Typical examples are the investigation on rapidly expanding plasmas or shock wave propagation in solids, the study of microscopic living cells and so on. Alternative techniques [Zholents *et al.*, 1995] are being investigated world-wide in order to achieve as short pulses of X-rays as possible.

Several years ago [Murnane *et al.*, 1989], sub-picosecond pulses of X-ray radiation were generated by the interaction of short, intense laser pulses with matter. Later, [Kmetek *et al.*, 1992], hard X-ray radiation was found to be generated in ultra-short pulse laser-matter interactions. Recently, several experiments [Nickles *et al.*, 1996; Chichkov *et al.*, 1996] have been devoted to the experimental study of ultra-fast X-ray emission from laser-plasmas and the interaction of high power femtosecond laser pulses with matter is now established as a powerful technique of generating short intense X-ray pulses with photon energies extending from a few hundreds of electronvolts to and beyond the MeV region.

As discussed in Chapter 3, the traditional collisional absorption mechanism is inefficient at the intensities considered here. In fact, analytical studies and numerical simulations show that collisionless processes including resonance absorption [Godwin *et al.*, 1993], vacuum heating [Brunel *et al.*, 1987] and anomalous skin-layer heating [Andreev *et al.*, 1992] are the key factors in the absorption of laser energy by the target. It has been shown that these absorption processes lead to non-thermal electron distribution functions. In particular, high intensity, ultra-short laser heating gives rise to the production of a substantial fraction of highly energetic electrons and a relatively cold background plasma. The energetic electrons are responsible, through collision with ions, of emission of high energy photons in a continuum spectrum while the background plasma can account for keV or sub-keV line or continuum emission.

The properties of the X-ray radiation emitted by femtosecond laser-matter interactions are mainly determined by the processes that account for absorption of laser energy by the target. In fact, when efficient coupling with solid targets occurs, solid density plasmas characterized by high temperatures are generated and X-ray emission in a broad spectral range takes place. As

discussed in detail in Chapter 4, X-ray photons are emitted either by radiative deexcitation and recombination processes or by electron-ion collisions (bremsstrahlung). Therefore, the duration of the X-ray pulses depends upon the transient properties of these radiative relaxation processes and upon the lifetime of energetic electrons produced during the laser-matter interaction process.

On the other hand, the properties of this radiation also depend upon the type of target with which the laser pulse interacts. In particular, the use of mass limited targets consisting of very thin foils, instead of thick (massive) targets, can give significant advantages in the production of short X-ray pulses. In fact, advanced numerical simulations and analytical scaling laws developed for femtosecond laser interaction with either solid or thin foils targets [Rosen, 1990] consistently predict significantly shorter x-ray pulses. In particular, X-ray pulse lengths comparable to the laser pulse length are predicted when thin targets are used in combination with high Z material. In this case, the target is considered thin when it is completely heated by the thermal wave during the laser pulse.

According to simple considerations on the propagation of thermal heat waves, it can be calculated that the the penetration depth is of the order of 500 Å in 100 fs. By following the simple condition that the target thickness be close to (less than) the heat penetration depth corresponding to the pulse-length considered, for a given target material, the duration of the X-ray pulse generated minimized. In fact, from the point of view of the X-ray radiation pulse-length, the condition for a rapid fall of the emission is that the radiation mean free path be much greater than the plasma scale-length. In the case of thin targets, once laser energy is absorbed as discussed above, and distributed over the whole target thickness, the foil immediately explodes and, consequently, its density rapidly drops leading to a rapid increase of the radiation mean free path. Consequently, the radiation emitted by radiative relaxation processes or other mechanisms as outlined above, can escape freely, without undergoing absorption and re-emission. Therefore, the emission process is rapidly concludes and the resulting X-ray pulse length is mainly determined by the intrinsic properties of emission mechanisms.

As pointed out above, the properties of X-ray emission strongly depend upon the absorption mechanism that account for substantial absorption of laser energy. In some cases, the absorption process has well known properties that enable to identify their contribution to the emission process.

In a recent experiment [Gizzi *et al.*, 1996], the role of resonance absorption in the interaction of high intensity femtosecond laser pulses with thin plastic foils was investigated by exploiting the dependence of this absorption mechanism on polarization of the incident laser light. The intensities of hard X-ray emission and the specularly reflected second harmonic (SH) of the laser frequency were measured as a function of the polarization of the laser light. While the observed features of the SH emission are a clear signature of the occurrence of resonance absorption, the intensity of the X-ray radiation was found to be very sensitive to the polarization, as expected by the resonant enhancement of the p-polarized electric field at the critical density typical of resonance absorption. The plot of Fig.xrayvspol clearly shows the dramatic dependence of X-ray yield as a function of the polarization angle. We observe that this result provides a direct way of controlling the intensity of the X-ray radiation in view of applications of similar experimantal configurations as X-ray sources.

5. X-RAY EMISSION AS PLASMA DIAGNOSTICS.

The study of plasma self-emission in the X-ray region is regarded as a primary tool for the investigation of plasmas generated in laser-matter interactions. Indeed, in the case of experiments designed to investigate laser-plasma coupling processes or hydrodynamic laser induced instabilities in the interaction with preformed plasmas, a detailed analysis of the spectral and spatial features of the X-ray emission allows a direct monitoring of the modifications induced by the interaction processes on plasma conditions (Afshar-rad T. et al, 1992).

As discussed previously, atomic physics processes are strictly related to the thermodynamic properties of the plasma. X-ray line emission from H-like and He-like ions can been investigated in order to study the temporal evolution of plasma properties such as electron temperature and electron density. Experimental line ratios between resonance emission lines from He-like and H-like Al ions can be compared with the analogous rates calculated in the appropriate plasma equilibrium model. On the other hand, X-ray imaging with high temporal resolution is also considered the key diagnostic technique to study basic interaction processes including, for example, absorption processes and thermal transport, or to monitor the dynamics in the implosion of inertial confinement fusion capsules (Budil K.S. et al, 1996).

5.1. X-RAY SPECTROSCOPY.

Time-resolving spectroscopic techniques

The temporal evolution of the electron temperature can be inferred by comparison of experimental line ratios with the predictions of the atomic physics simulation codes based upon *collisional-radiative* equilibrium as discussed in Sect.4. As an illustrative example of experimental temperature measurements from laser produced plasmas we will consider plasmas generated by exploding Aluminium targets. In these plasmas strong line emission from highly stripped Al ions, namely, He-like and H-like Aluminium ions, occurs. The wavelength and the corresponding photon energy of the most intense resonance lines from these ionic species and the corresponding notation used in the remainder of this paper are reported in Table.I.

He	l(Å)	hn(eV)	TRANS.	H	l (Å)	hn(eV)	TRANS.
Heα	7.75	1600	$1s^2$ - 1s2p	Lyα	7.17	1729	1s - 2p
Heβ	6.64	1867	$1s^2$ - 1s3p	Lyβ	6.05	2050	1s - 3p
Heγ	6.31	1965	$1s^2$ - 1s4p	Lyγ	5.74	2160	1s - 4p
Heδ	6.17	2010	$1s^2$ - 1s5p	Lyδ	5.60	2214	1s - 5p
Heε	6.10	2032	$1s^2$ - 1s6p	Lyε	5.53	2242	1s - 6p

Table I. Wavelength and photon energy of resonance lines from He-like and H-like Aluminium. The resonance series of H-like Al ions is labelled according to the analogous Lyman series of the Hydrogen atom.

Since the x-ray source is very small, typically <<1mm, and extremely bright, a simple x-ray spectrometer consisting of a flat crystal set in a first order Bragg configuration can be employed to perform spectral analysis in the wavelength range from 10Å down to ≈1 Å. Due to the short duration (<≈ns) of the X-ray emission, its temporal evolution can only be studied by means of an X-ray streak-camera fitted with X-ray sensitive photo-cathodes coupled to the spectrometer. **Fig.1** shows a schematic set-up of a TlAP ($TlHC_8H_4O_4$) crystal ($2d = 25.9$ Å) for x-ray spectroscopy of Al laser plasmas in the 5-8Å spectral range, where K-shell emission from He-like and H-like Al ions occurs.

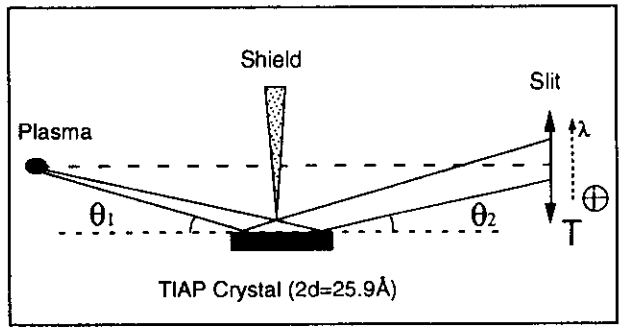

Fig.1. Schematic of flat TlAP crystal configuration in the X-ray spectrometer for time-resolved spectroscopy measurements of highly ionized Al plasmas.

The temporal resolution of the time-resolving spectrometer is determined by the width of the slit in front of the streak-camera cathode and can be as high as a few picoseconds. The spectral resolution is basically due to the size of the emitting region and can be evaluated with a simple calculation assuming a

plasma emitting region whose size is that given by the cross-section of the plasma along the line of sight of the spectrometer. This value can then be compared with the experimental one obtained directly from wavelength calibrated X-ray spectra. In the case of plasma sizes of the order of few hundreds of microns, resolving powers of up to 10^4 can be obtained.

5.2. PLASMA TEMPERATURE

Some illustrative experimental results

Fig.2 shows a typical time-resolved spectrum obtained from a plasma produced by laser irradiation of a thin disk Al target at a total intensity of 6.5×10^{13} W/cm^2 while **Fig.3** shows a 1D trace taken 500 ps after the peak of X-ray emission and integrated over 50 ps, which was the temporal resolution of the spectrum. Emission lines from the Heβ to the Lyδ are clearly visible with the Lyγ and Lyδ emerging from the He-like continuum. The Heε line is just visible as a shoulder-like feature on the long wavelength side of the Lyβ line.

Line intensity profiles were found to be well fitted using gaussian profiles with $\Delta\lambda_{FWHM}$ = 40mÅ ± 10%. Except for the Heε and Lyβ lines all remaining lines are well resolved and it is therefore relatively simple to determine the line intensity. With the available spectral resolution, the Lyβ line is only partially resolved, being merged with the Heε and higher quantum number He-like lines and with the He-like continuum edge. Intensity ratios involving the Lyβ transition will consequently be affected by a larger error. A better condition from this point of view can be accomplished at higher heating laser intensities as hotter plasmas are generated with more intense H-like lines. This effect is clearly shown in **Fig.4** which shows a time-resolved spectrum obtained in similar conditions as Fig.2 but with a heating laser intensity of 1.2×10^{14} W/cm^2.

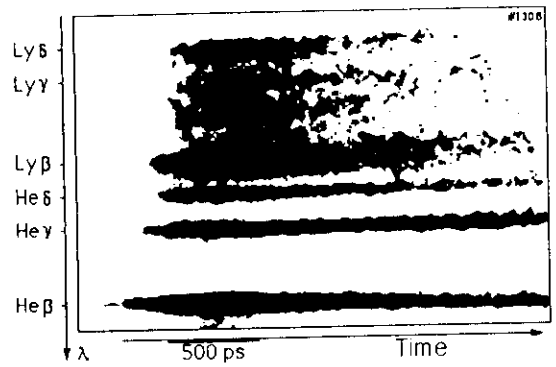

Fig.2. Time-resolved X-ray spectrum of K-shell Aluminium emission from plasma heated at an irradiance of 6×10^{13} W/cm^2 by four 600ps FWHM, 1μm laser pulses.

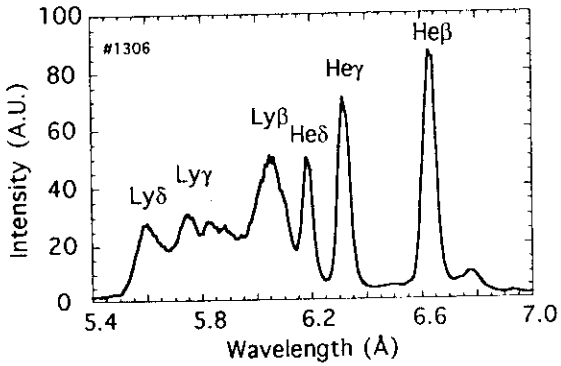

Fig.3. Lineout of the spectrum of Fig.2 taken 500 ps after the peak of X-ray emission intensity and integrated over 50 ps, i.e. over the temporal resolution of the spectrum.

Also visible in this spectrum is the X-ray emission arising from a delayed interaction laser pulse set to reach the plasma 2.5 ns after the peak of primary heating pulses. The effect of the delayed interaction on the conditions of the preformed plasma will be discussed in detail later in this section. However, it is important to notice that the spectral resolution for this part of the spectrum is clearly improved due to the smaller spatial extent of the X-ray source. In fact, in this case, the X-ray emission comes from the region of plasma heated by the interaction beam whereas the initial part of the spectrum comes from the whole plasma extent.

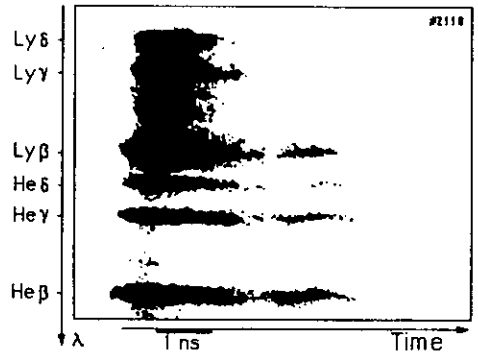

Fig.4. Time-resolved X-ray spectrum of K-shell Al emission from plasma heated at an irradiance of 1.2×10^{14} W/cm^2 by four 600 ps FWHM, 1μm laser pulses. The effect of the interaction pulse delayed by 2.5 ns with respect to the peak of the heating pulse is also visible.

The effect of the higher heating intensity compared to the spectrum of Fig.2, and the consequent increase of the electron temperature is shown by the stronger Lyγ and Lyδ lines which now clearly emerge from the He-like continuum. These circumstances make X-ray spectra like this, obtained at higher laser intensities, more suitable for temperature measurements from line intensity ratios between H-like and He-like Al lines. On the other hand, the conclusions on the electron temperature obtained in these conditions can be reliably extended to the regime of lower heating laser intensities by comparing the experimental results with the hydrodynamic numerical simulation. The Lyγ to Heγ intensity ratio of the spectrum of Fig.4, restricted to the heating phase only, has been measured as a function of time and the result is shown on **Fig.5**.

The *zero* of the temporal axis corresponds to the time at which the He-β line, that is the most intense line in the spectrum of Fig.4, reaches its maximum. Incidentally, we notice that the lines shown in the spectrum, reach their peak approximately simultaneously. Only a small difference can be detected between the set of the He-like lines and the set of the H-like lines, the latter peaking a few tens of picoseconds later. This particular choice of origin for the temporal axis will be justified by the analysis presented later in this section. In fact, according to the simulation, the peak of the X-ray emission is very closely related to the peak of the heating laser pulse, which is the main temporal *fiducial*.

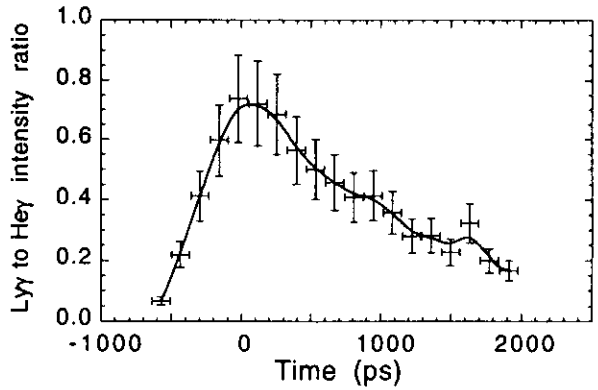

Fig.5. Experimental intensity ratio of the H-like Al γ-line (1s - 4p) to the He-like Al γ-line ($1s^2$ - 1s4p) as a function of time with respect to the peak of the He-like Al *b*-line.

As already pointed out, spectra like that shown in Fig.4 result from spatial integration over the whole plasma extent. Consequently plasma parameters determined by analysis of line emission spectra should, in principle, be regarded as averaged over plasma electron temperature and density distribution in space. However, once plasma expansion takes place and laser energy is absorbed throughout the plasma, thermal condiction ensures that a uniform temperature can be established over the whole plasma extent.

On the other hand, during the initial stage of plasma formation, highly localized heating in the proximity of the critical density takes place and most of x-ray emission originates from this region. Therefore, though time integrated, the kind of measurement shown above provides a nearly complete knowledge of electron temperature in the plasma regions of interest.

5.3. PLASMA OPACITY.

Opacity effects in temperature measurements

In order to minimise the contribution of opacity effects, it is always preferable to restrict the analysis of line intensity ratios to high quantum number members of a resonance series which are less sensitive to reabsorption effects. On the other hand, line intensity decreases dramatically going towards high quantum number members resulting in low signal to noise ratios.

Therefore, the final choice will be a compromise between these two limits. However as described below, although, generally speaking, opacity effects play an important role in x-ray emission processes, their contribution to a selected choice of emission lines can be once again restricted to the early phase of plasma formation, when hot, high density plasma is generated.

Recalling the previous example of temperature measurements, the intensity ratio between Lyγ and Heγ was calculated for a uniform plasma as a function of the electron density and temperature and for an optically thin plasma.and for optically thck plasmas where plasma columns of 10 μm and 100 μm were considered. The results of such a calculation are shown in **Fig.6** for densities ranging from 10^{18} to 10^{22} cm^{-3} and for temperatures from 380 to 800 eV. We notice that, for densities below a few times $10^{19}cm^{-3}$ the intensity ratio is almost independent of both density and opacity effects. However, in the range of densities between a few times 10^{19} cm^{-3} and a few times 10^{21} cm^{-3}, there is a strong dependence of line ratios upon density. Also opacity effects strongly affect line ratios only for densities above $10^{20}cm^{-3}$.

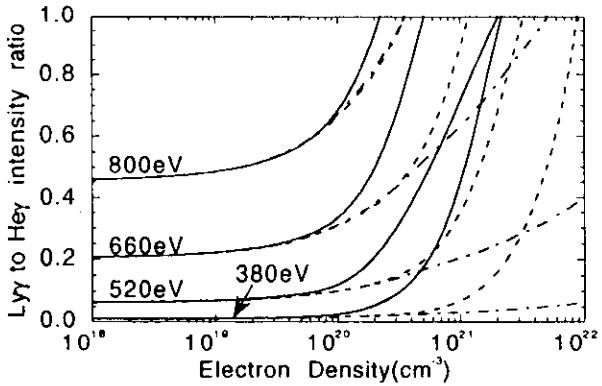

Fig.6. Lyγ to Heγ intensity ratios as a function of electron density for different electron temperatures. Solid line curves have been obtained with no opacity included in the calculation while dashed line and dashed-dotted lines correspond to calculation with opacity effects included and with 10 μm thick and 100 μm thick plasma respectively.

According to these results, electron density and opacity are expected to play a dominant role in determining intensity ratios during the explosion of the target when the density is high. Later in time, i.e. few nanoseconds after the peak of the laser pulse, plasma conditions will be such that opacity effects will affect the Lyγ to Heγ intensity ratio only slightly. Once the density of the plasma is known, a plot like that of Fig.6 can be used to convert line ratios in electron temperatures. **Fig.7** shows the temporal dependence of the electron temperature obtained by comparing the experimental intensity ratios of Fig.5 with the plot of Fig.6. Each curve of the graph was obtained comparing the experimental ratio with the calculated one and assuming an opacity effect with a given length of homogeneous plasma and looking for the electron temperature at which agreement between experiment and theory was achieved. The same procedure used for the three plasma lengths taken into account in Fig.6.

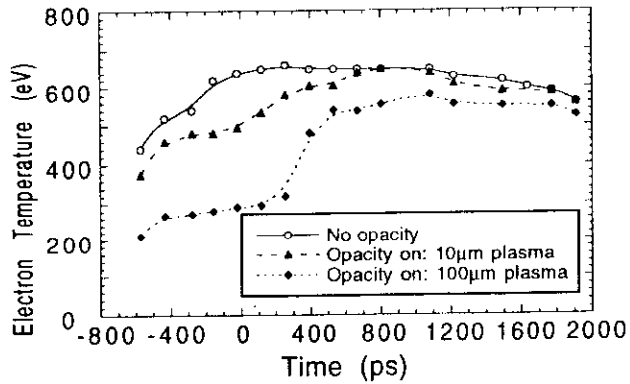

Fig.7. Temporal evolution of the electron temperature of the plasma obtained comparing the experimental intensity ratio of Lyγ to Heγ with the prediction of the steady-state Collisional Radiative numerical code RATION.

As already observed, opacity effects give a major contribution during the pulse while later than about 1 ns after the peak of heating pulses, the three curves approach each other and give a well defined electron temperature within less than 100 eV. In particular, at 2 ns, when the electron density is of the order of a tenth of the critical density, the values of the three curves agree within less than 50 eV, giving an average electron temperature of 550 eV, the error being less than 8%.

Laser re-heating of preformed plasmas

It is instructive to examine the effect of a high intensity laser pulse focused on a preformed plasma. A great deal of information can be gained from

spectroscopic analysis of the X-ray radiation emitted during the heating process as well as from X-ray imaging studies. In this section we will discuss the first method while the imaging technique will be introduced in the following.

When a laser pulse strikes a long scalelength preformed plasma, energy is absorbed locally and gives rise to a rapid re-heating of the plasma with intense re-emission of X-ray radiation. A typical example of plasma re-heating has already been shown in **Fig.4** and can be more clearly observed in the spectrum of **Fig.8** where the first x-ray emission peak generated during plasma production by laser explosion of a small Al disk is followed by a second emission peak due to the interaction of a second laser pulse focused on the plasma generated by the first.

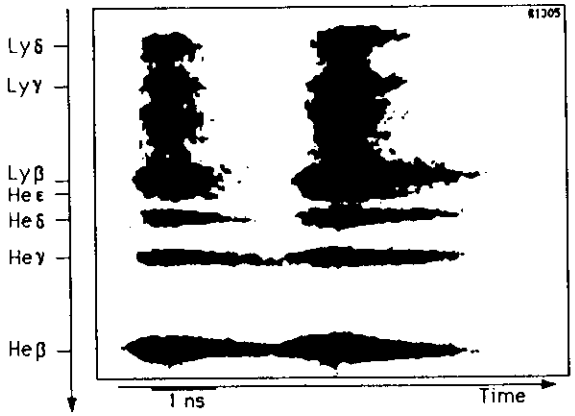

Fig.8. Time-resolved X-ray spectrum of K-shell Aluminium emission from plasma heated at an irradiance of 1.2×10^{13} W/cm^2 by four 600 ps FWHM, 1μm laser pulses. The interaction beam was focused on the plasma in a 800 μm by 100 μm line focus at an intensity of 3.0×10^{14} W/cm^2 and was delayed by 2.5 ns with respect to the peak of the heating pulse.

Fig.9 shows the temporal evolution of the electron temperature obtained from the spectrum of Fig.9 relative to the interaction phase. Due to the high intensity of the second laser pulse, strong line emission up to Lyδ and Heδ was detected and therefore, the electron temperature could be measured taking into account the Lyg to Heg intensity ratio as well as the Lyd to Hed intensity ratio.

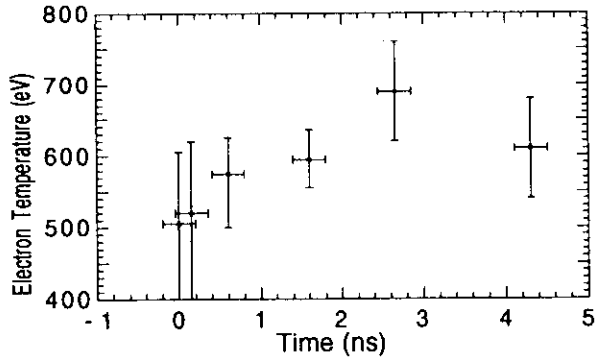

Fig.9. Temporal evolution of the electron temperature of the plasma region heated by the interaction pulse obtained comparing the experimental intensity ratio of Fig.8 with numerical calculations.

This plot shows the change in the electron temperature induced by the delayed interaction pulse. In fact, in the conditions considered here, the delayed laser pulse interacting with an underdense plasma can give rise to an increase of the electron temperature in the interaction region of up to 200 eV. These circumstances should be carefully considered as they can play a very important role in the interaction physics and in particular on the dynamics of laser induced instabilities.

5.5. X-RAY IMAGING OF PLASMAS

Basic X-ray Imaging techniques

A description of the techniques used to study X-ray emission from plasmas by means of time-resolved imaging will be given in this section.

Due to the strong X-ray emissivity of laser produced plasmas, a simple imaging device consisting of a pin-hole camera (PHC) can be employed to obtain X-ray images of the plasma. Such images can be recorded directly by using X-ray sensitive detectors (windowless CCD cameras, X-ray films) or by employing phosphor screens coupled to optical image intensifiers. Presently available intensifiers based on the microchannel-plate (MCP) (Wiza L., 1979) technology can easily provide a thousand-fold overall gain in intensity. Ordinary CCD cameras or commercial photographic B&W film can then be used to record the intensified image.

Both magnification and resolution of such a device can be easily calculated from simple geometrical consideration. According to the geometry of Fig.10 the magnification of a pin-hole camera is given by $M = A'/A = q/p$. The spatial resolution of the image is generally given by the combination of geometrical and diffraction effects. It is easy to verify that the size of the image of a point source in the geometrical limit is given by $\Delta x_g \cong d_{ph}(1+M)$, d_{ph} being the pin-hole diameter. According to the Fraunhofer diffraction theory (Born & Wolf, 1970), the typical transverse size of the Airy pattern produced by a uniformly illuminated circular aperture of diameter d_{ph} at a distance q, i.e. the diameter of the circle containing 85% of the total energy, is $\Delta x_d \cong 2.44\, q\lambda/d_{ph}$, λ being the X-ray wavelength. The best pin-hole size is given by the condition $\Delta x_g = \Delta x_d$, that is,

$$d_{ph} = \sqrt{\frac{2.44\,\lambda\, q}{1+M}}. \qquad (1)$$

For typical conditions of laser-plasma experiments, $\lambda \approx 5$Å, and $q \approx 50$cm, the best pin-hole diameter is approximately 7 μm for $M \approx 10$ and 5 μm for $M \approx 30$. On the other hand a lower limit to the pin-hole size that can be employed in laser-plasma experiments is also set by the available X-ray flux as well as by the manufacturing feasibility. Typical commercially available pin-holes have diameters as small as 5 μm. Therefore, for a magnification $M < 30$ the image resolution is determined by the geometrical limit. The size of the smallest feature which can be resolved in the object plane, i.e. in the plasma, is then

$$\Delta x_{plasma} \cong d_{ph}\left(1+\frac{1}{M}\right). \qquad (2)$$

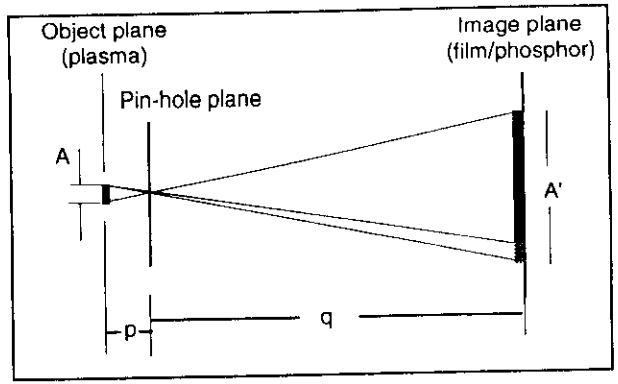

Fig.10 Geometry of a pin-hole camera for X-ray imaging of plasmas. The pin-hole diameter determines the spatial resolution of the image. In the limit of high magnification the spatial resolution of the image in the object plane is simply given by the pin-hole diameter itself.

In the limit of high magnification the spatial resolution of the pin-hole camera image in the object plane is given by the pin-hole diameter. The pin-hole diameter also determines the X-ray flux collected by the camera.

The number of 1KeV photons reaching the recording device per unit area of the magnified image can be written as follows

$$\Phi_{1keV} = 6.25\times10^{15}\,\frac{\eta_x E_L d_{ph}^2}{16\pi q^2 M^2 A^2}\ \text{photons / cm}^2 \qquad (3)$$

E_L being the laser energy absorbed by the plasma in Joules and η_x being the X-ray conversion efficiency. In the conditions of our experiments the absorbed laser energies E_L range from several joules to hundred joules and the X-ray conversion efficiency in the 1KeV region is of the order of $\eta_x \approx 0.1$. With a plasma transverse size $A \approx 100$ μm and assuming an image magnification $M = 10$, with a 10 μm pin-hole diameter and a pin-hole to image distance, $q \approx 50$cm, we obtain an X-ray flux ranging from 10^5 to 10^8 photons / cm^2.

This value should be compared with the flux required to obtain an optical density above fog of $D = 1$ on a typical X-ray film (Rocklett et al., 1985), that

is, approximately $\Phi_{1keV} = 10^8$ photons / cm^2. Therefore the use of an active (intensified) pin-hole camera becomes necessary in these experiments in order to cover the whole range of experimental conditions.

Spectral selection in X-ray imaging

Time integrated imaging is usually employed as a basic monitor of the quality of the laser-matter interaction process. However, when appropriate spectral selection is performed, valuable information on the physics of the interaction can also be gained. To illustrate the role played by spectral selection in laser produced plasma studies we describe an experiment carried out by using a pin-hole camera to study the interaction of high intensity picosecond laser pulses with layered-targets. The PHC was fitted with a four-pin-hole array, thus resulting in a simultaneous 4-channel imaging device. Each channel was sensitive to different spectral regions due to the different X-ray filters used. One channel was filtered with a 20 μm thick Be filter, while the other three channels were additionally filtered with 3 μm Al, 8 μm Cu, and 3 μm Al+8 μm Cu respectively. The transmittivity of a 25 μm Be, 3 μm Al and 8 μm Cu foil is plotted in **Fig.Filter** as a function of the X-ray photon energy in the range from 100 eV to 100 keV, calculated using available (Henke et al., 1985) mass absorption coefficients.

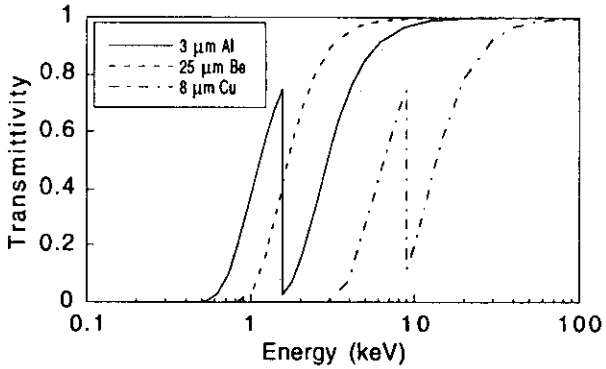

Fig.Filter. X-ray transmittivity of a 3 μm thick Al foil, a 25 μm thick Be foil and a 8 μm thick Cu foil calculated using tabulated mass absorption coefficients.

According to Fig.Filter, the imaging channel filtered with the Be foil is therefore sensitive to photon energies above ≈1.5 keV. The addition of the Al filter in the second channel further shifts this lower bound to approximately 2.5 keV. In the case of X-ray emission from Al plasmas, the Al filter also cuts off most of the line emission from highly ionized Al ions, as already shown in Fig.4.4.4. The second and the third imaging channels are mainly characterized by the transmittivity of the Cu foil. In this case the presence of the L-shell absorption at 933 eV selects photon energies between ≈6 keV and 9 keV and greater than ≈15 keV.

The effect of the different filtering conditions on the image of the X-ray plasma sources is shown in **Fig.PHCProfiles**. The plasma was produced irradiating a layered target consisting of a solid plastic (Mylar) target coated with a 0.1 μm thick Al layer and overcoated with a 0.1 μm thick plastic (CH) layer. The laser beam focal spot, calculated by direct obscuration techniques, was ≈25 μm in diameter and the intensity was 3.6×10^{16} W/cm^2. The plots of Fig.**PHCProfiles** were obtained from one-dimensional line-outs taken along the diameter of each of the four disk-shaped X-ray images. The horizontal axis is labelled in terms of the distance on the target plane.

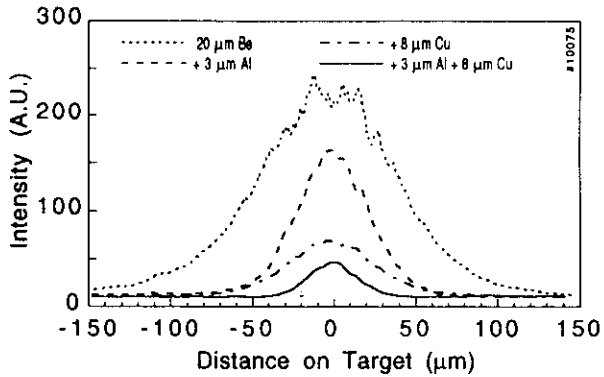

Fig.PHCProfiles. Lineout of four differently filtered X-ray images obtained from a single interaction event using a pin-hole camera fitted with a 4-pin-hole array. The plasma was produced by irradiating a solid plastic (Mylar) target coated with a 0.1 μm thick Al layer, overcoated with a 0.1 μm thick plastic (CH) layer. The laser intensity was 3.6×10^{16} W/cm^2 in a ≈25 μm diameter focal spot.

The FWHM of the profile relative to the Be filtered channel is approximately ≈90 μm while the Be+Al and the Be+Cu both give a FWHM of 60 μm. Finally the Be+Al+Cu channel gives a FWHM of 30 μm. According to these results the extent of the X-ray emitting region, in the case of the

Be+Al+Cu channel, is slightly larger that the 25 μm diameter focal spot of the laser. On the other hand, only very energetic X-rays contribute to the image taken in these conditions. Such x-rays can only be produced by continuum emission, bound-bound processes being energetically limited to the maximum transition energy of the mostly ionized atom present. In the particular case considered here, the maximum bound-bound transition energy in H-like Al ions, is given by the ionization energy of the H-like Al ion which is ≈2.3 keV, that is well below the lower energy bound of ≈6 keV set by the transmittivity of the Cu filter.

Continuum emission, and in particular that arising from free-free transitions (bremsstrahlung), is directly related to the electrons heated by the laser electric field and, therefore, provides a good indication of the actual extent of the laser intensity distribution on target.

In contrast, the FWHM of the profile taken with the 8 μm Cu filter only is 60 μm, i.e. two times larger than the 30 μm considered above. Moreover, the result obtained with the Be filter only, which gives a FWHM of ≈90μm is three times larger than the FWHM obtained when the Al filter is added to the Be filter. These results indicate that the region immediately outside the laser focal spot exhibits a strong X-ray emissivity in the spectral range between ≈1.5 and ≈3 keV, where the Al filter mainly contributes to the attenuation, due to the K-shell absorption edge at 1560 eV. This emission is most likely due to the Al layer of the target that give rise to line emission from bound-bound transitions in He-like and H-like Al ions. Whether this region is directly heated by the laser energy present in the *wings* of the focal spot intensity distribution, or is heated due to lateral electron heat conduction is still an open issue. However, in general, it is likely that both effects contribute to distribute the laser energy over the observed region.

Time resolving techniques

Temporal resolution can be achieved by forming the X-ray image generated by the PHC on a position sensitive time resolving device. By using an X-ray streak camera, temporal resolution up to the picosecond range can be obtained. However the spatial information is restricted to the direction perpendicular to the streak direction (1-D time-resolved imaging). This technique has been successfully employed for several years (Willi O., 1988) and is very useful when a continuous mapping of the temporal evolution is required. However, two-dimensional position sensitive devices with a temporal resolution as high as a few tens of picosecond based on *microchannel-plates* (MCP) (Kilkenny J.D., 1991) can now be employed. MCP's are characterized by a very low capacitance that enables fast switching of the externally applied electric fields. These devices can therefore be used as *gated intensifiers* as well as a DC intensifiers and usually do not require additional intensifiers due to their intrinsic high gain.

In all the applications considered above, in order to avoid motional blurring of the images, framing times as short as few tens of picoseconds are often necessary. Recently, X-ray framing-times as short as 30-40 ps have been reported (Bradley D.K., 1995). On the other hand, the scalelength of the features of interest can be as small as few microns, thus requiring spatial resolutions as high as a few microns. Furthermore, another important feature of such imaging systems is the number of frames that can be recorded on a single interaction event, so that the temporal evolution can be mapped with sufficient accuracy. The final configuration is therefore a trade-off between scientific requirements, spatial, temporal and spectral accuracy on one side, and flexibility, reliability, and ease of use in on the other side.

In the following we describe the implementation of a multi-frame X-ray imaging device with high temporal resolution for the study laser-plasma coupling processes. The interaction of a high intensity laser pulse with preformed plasmas, as already discussed above from the point of view of X-ray time resolved spectroscopy, is investigated by means of time resolving imaging device.

The X-ray detection unit (Kentech Inst. Ltd) was based on MCP that enabled four-frame X-ray imaging with 140 ps gate-time and inter-frame time adjustable from zero to a few nanoseconds. A diagram of the sensitive unit is shown in **Fig.11**. The input surface of the microchannel-plate detector was coated with a 500nm copper layer in four separated rectangular regions (Strip-Lines) acting as photocathodes while the output surface was uniformly coated with a thin copper layer.

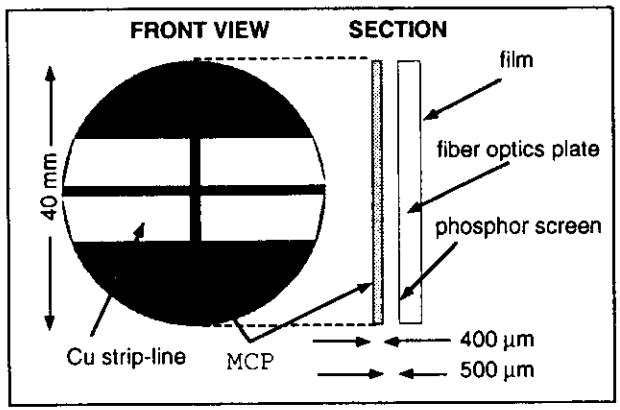

Fig.11 Schematic arrangement of the X-ray Imager detection system with the MCP input surface showing the four 500 nm thick Cu coated regions. (Kentech Instr. Ltd., UK)

Each strip-line could be activated independently by a high voltage pulse. Photons incident on one of the activated strip-lines generates photoelectrons that, accelerated by the external electric field, hit the walls of the micro–channel producing secondary electron emission. This process takes place several times during the flight of the electrons in the micro–channel resulting in a photomultiplier-like gain. The electrons produced are finally driven onto a phosphor screen by a second electric field. Due to the small electron path lengths (see Fig.11), a relatively large electric field is capable of preserving the spatial distribution of the outcoming electrons. A standard B&W film records the light produced by the phosphor screen and collected by a fibre optic bundle plate.

A specifically designed PHC equipped with a 4-pin-hole array capable of producing four identical images of the object plasma onto the four sensitive strip-lines of the MCP was employed. The PHC magnification in the experiment described below was 13X with a pin-hole size of 10 μm. Both magnification and pin-hole size were chosen in order to resolve details of about 10 μm in the plasma.

The x-ray radiation collected by the PHC is the filtered in order to block visible radiation and to enhance the sensitivity of the detector to the spectral range of interest. As we pointed out above, time resolving imaging can be successfully employed in the investigation of the modifications of plasma condition induced by local laser energy deposition. To this porpose continuum emission is a more sensitive than line emission. In fact, continuum radiation and, in particular, radiation originating from free-free processes, is closely related to the conditions of the electron population and is only coupled to the ions via their charge number and the electron-ion collision frequency. In contrast, the properties of line radiation are strongly related to the particular equilibrium holding in the plasma, as well as to ion relaxation processes.

The contribution of resonance line emission from hot Al plasma can be strongly depressed in favor of the underlying continuum simply by using a thin Al filter. In fact, due to the Al K-shell absorption edge at ₁560 eV, most of the line emission from He-like and H-like Al ions is strongly absorbed by the Al filter. Therefore the dominant component of the transmitted X-rays will be continuum radiation originating from free-bound and free-free transitions in He-like and H-like Al ions, as discussed above.

7. Comparison of the main X-ray sources.

Before carrying up the comparison between the performances of the different X-ray sources, we have to shortly consider two further sources, which do not fit the classification of X-ray plasma sources: conventional X-ray tubes and synchrotron radiation.

7.1. X-ray tubes.

In a X-ray tube a beam of electrons, accelerated in an electric field up to several tens of KeV energies, impinges on a metal anode. The electron impact on the target produces Bremsstrahalung continuum, and inner shell emission. The spectrum of the Bremsstrahlung continuum essentially depends on the value of the accelerating electric potential, while the spectrum of the shell emission depends on the electric potential and the anode material.

These incoherent X-ray sources have been, up to the early1950 years, the only available for the research and applications. Today they are still employed in medicine diagnostic and in the applications that require a CW X-ray source.

The spectral brightness of the conventional X-ray tubes can vary of at least two order of magnitude, among stationary-anode tubes (lower end of range), rotating-anode tubes (middle), and rotating-anode tubes with micro focusing (upper end of the range). Moreover, due to their spectral sharpness, the line emission can overcome the continuum up to a ten thousand factor. For the Cu K-shell emission a spectral brightness up to 10^{10} photons s^{-1} mm^{-2} mr^{-2} (0.1% bandwidth)$^{-1}$, can be attained.

The spectral brightness is the most relevant X-ray beam figure of merit. It represents the photon flux per unit solid angle in a bandwidth $\Delta\lambda/\lambda=10^{-3}$.

7.2. Synchrotron radiation.

The synchrotron radiation was first observed as a parasitic emission from an electron synchrotron accelerator (Elder F.R., 1947) and since the initial observation many accelerator facilities have been built to provide this kind of radiation for scientific purposes and applications. This radiation is produced when electrons, constrained by means of a magnetic field to follow a circular orbit, suffer a radial acceleration. The radiation emitted by an electron beam of relativistic energy circulating in ultra-high vacuum is extremely powerful into the X-ray range. Moreover this radiation is strongly directional in the forward direction tangential to the electron orbit, and is highly polarised in the plane of the orbit. The radiation natural opening angle, in the vertical plane, is

$$\psi=\frac{1}{\gamma}=\frac{m_0c^2}{E},$$

while the horizontal divergence of the radiation is determined by the width of the slit used to defines the angle $\Delta\theta$ from which radiation is taken. In the previous equation m_0 is the electron rest mass and E the beam energy.

Usually the synchrotron radiation facilities have been constructed around storage rings. In a storage ring, an electron beam, pre-accelerated by a linear accelerator followed by a synchrotron accelerator, is injected and accumulated, up to a few hundred mA current. The storage ring is an ultra-high vacuum tube consisting of arcs of circle joined by straight sections. In the turning points are placed high magnetic field dipole bending magnets, which keep the electrons in their orbit. At the turning points white light is generated, which is extracted through gaps in the magnet yokes. The radiation impinging on a grazing incidence grating is frequency selected by a slit and then used at the experiment station. In the straight sections of the ring the RF cavities are placed, which replenish the electron beam energy lost by radiation, and quadrupole magnets for the beam focusing and control. The RF accelerating cavities produce the bouncing of the electron beam into short packets of current. So, synchrotron radiation is in the form of a continuous train of pulses (50-500 ps), separated by longer periods of time (2ns-1μs), depending on the ring parameter.

The spectrum of the radiation extracted from a bending magnet is a continuum, similar in shape to that of a blackbody. To characterise this spectrum it is useful to introduce a critical wavelength λ_c, defined as the wavelength which has half the emitted power above and half below it. The spectrum maximum is at $\lambda_{max}=2\lambda_c/3$ and, for fully relativistic electron beam, the following relationships hold:

$$\lambda_c=\frac{20.7}{\rho^2B^3}$$

$$B\rho=\frac{E}{300}$$

In the two previous equations, λ_c(nm) is the critical wavelength, ρ(m) is the magnetic bending radius, B(T) is the magnetic bending field and E(MeV) is the electron energy. For typical values of a storage ring, B=1 tesla, ρ=5m; so the electron energy come out E=1.5GeV, while the critical wavelength λ_c=0.8nm.

The quite large dimension (several meter in diameter) and cost of a conventional storage ring for synchrotron radiation make this source suitable only for large centrally operated facilities. However, the use of higher field (≈5tesla) super conducting magnets allows to reduce the size of the storage ring to a few meter in diameter. The reduced dimensions make this synchrotron radiation sources accessible also for smaller research laboratories.

In the straight sections of a storage ring are usually inserted periodic magnetic structures conceived to enhance the brightness in XUV emission region: the wavelength shifter, the wiggler and the undulator. These insertion devices produce oscillations of the electron beam in the plane of its path as it travels through the magnetic structure.

The wavelength shifter consists of a three pole magnet with a magnetic field much stronger than a bending magnet. As a consequence of the stronger magnetic field the critical wavelength is shifted to a shorter value, even if the source brightness stays the same.

The other two insertion devices (wiggler and undulator), being multipole magnetic structures inducing on the electron beam several oscillations, are capable of increasing the source brightness. The magnetic field, orthogonal to the orbit plane, varies along the insertion device as

$$B(z) = B_0 \cos\left(\frac{2\pi z}{\lambda_u}\right)$$

where B_0 is the amplitude of the magnetic field and λ_u its spatial period. The parameter characterising the electron motion in the insertion device is the deflection parameter

$$K = \frac{eB_0\lambda_u}{2\pi m_0 c} = 93.4 B_0(T)\lambda_u(m).$$

The maximum angular deflection of the orbit is

$$\delta = \frac{K}{\gamma}.$$

For $K \geq 10$ the angular deflection of the electron exceeds the natural opening angle of synchrotron radiation ($1/\gamma$). In these conditions the insertion device (called wiggler) is equivalent to a sequence of bending magnets of alternating polarity, whose radiation adds incoherently giving an overall brightness 2N times higher than a single bending magnet; N being the number of the magnet periods.

For $K \leq 1$ (undulator) the radiation from the different magnet periods is partially coherent and, because of the interference, is spectrally compressed into a series of narrow peaks at on-axis wavelength

$$\lambda_n = \frac{\left(1+\frac{K^2}{2}\right)\lambda_u}{2n\gamma^2}.$$

$$n = 1,3,5,...$$

The wavelength of the peaks can be tuned by varying different undulator parameters, such as B_0 and λ_u. For very small values of δ the brightness of the undulator can be enhanced by a factor up to N^2 compared with a single bending magnet of the same magnetic field. The undulator radiation is highly collimated and is almost laser-like. The spectral purity of the resonances and the half angle divergence of the radiation is:

$$\left(\frac{\Delta\lambda}{\lambda}\right)_n = \frac{1}{nN}$$

$$\vartheta \approx \frac{1}{\gamma\sqrt{N}}$$

Let us consider the radiation from a synchrotron source (LBL. Rep.,1986), operating with a 1.3GeV, 400mA electron beam; bending magnet field of 1.2T; wiggler field of B_0=2.3T; undulator field B_0=0.57 T, 142 poles, λ_u=0.035m. Typical values of the spectral brightness, in the energy range 0.1-5 KeV, are 10^{15} photons s^{-1} mm^{-2} mr^{-2} (0.1% bandwidth)$^{-1}$ for the bend magnet source, 10^{16} for the wiggler, $10^{17\text{-}18}$ for the undulator.

7.3. X-ray source comparison.

The comparison can be performed by considering the average and peak spectral brightness of typical sources of the different kinds, in the spectral range 1-10^5eV; see Fig. (1) and Fig. (2), respectively (Kirz J., 1986), (O'Neil F., 1988). As typical synchrotron source we shall consider the Advanced Light Source (ALS) machine, operating at the Laurence Berkeley Laboratory in the USA (LBL, 1986). As typical X-ray laser sources we shall consider a commercial high average power KrF excimer laser (100W average power, 0.5J, 25ns pulses at 200Hz repetition rate) focused onto high Z target (e.g. W or Au) at peak pulse irradiance of $I \approx 10^{12} W/cm^2$; and, for the peak power comparison, a KJ-class Nd laser (sub-ns pulse duration) as that operating at Laurence Livermore National Laboratory (LLNL) in the USA (Matthews D.L., 1983).

For what concerns the average spectral brightness, we can see that the brightness of continuum of X-ray tubes is four order of magnitude lower than plasma continuum, while the line emission can attain comparable values. However the spectral range of X-ray tubes emission is displaced at higher energies. The storage ring source is sizeably brighter than the repetitive laser-plasma source (the undulator being 10^4 time brighter than

the bend magnet). However, the X-ray laser-plasma source can be very attractive as a low cost laboratory X-ray continuum generator in the 1-10KeV spectral range. In particular in the experiment in which the X-ray source have to be synchronised with other repetitive light source. The high order harmonics exhibit a brightness few order of magnitude higher than X-ray laser-plasma continuum. In fact the lower conversion efficiency is largely overcome by the narrower bandwidth. However the conversion efficiency of the laser radiation into harmonics dramatically decreases at wavelengths shorter than 100 Å.

In the pulsed X-ray regime, the peak spectral brightness of the laser-plasma continuum exceeds that from the bent magnet source. The undulator emission stay four order of magnitude brighter than the X-ray laser-plasma source. The X-ray laser, operating on the 20.6nm line of the Ne-like Se ion, excited in a laser-produced plasma, is 10^3 time brighter than the undulator source. In these regime the X-ray tubes show a peak spectral brightness several orders of magnitude lower than the other available sources. Also the high harmonics are not interesting. At so high laser intensity regime they can generated only from laser-produced plasmas, with a conversion efficiency still too low.

References

Afshar-rad T., Gizzi L.A., Desselberger M., Khattak F., Willi O., Phys. Rev. Lett. **68,** 942 (1992)

Bastiani S., Giulietti D., Giulietti A., Gizzi A., Ceccotti T., Macchi A., Laser Particle Beams, **13** (1995) 493.

Biancalana V., et al Europhys. Lett., **22** (1993) 175.

Born and Wolf 1970

Bradley D.K. , Bell P.M., Landen O.L., Kilkenny J. D., Oertel J., Rev. Sci. Instrum. **66**, 716 (1995).

Brunel F., Phys. Rev. Lett., **59** (1987) 52.

Budil K.S., Perry T.S., Bell P.M., Hares J.D., Miller P.L., Peyser T.A., Wallace R., Louis H. , Smith D.E., Rev. Sci. Instrum. **67**, 485 (1996).

Charker M. et al, Proc. SPIE, **733** (1986) 58.

Davis G.M., Gower M.C., O'Neill F., Turcu I.C.E., Appl. Phys. Lett., **53** (1988) 1583.

Dawson J., Oberman C., Phys. Fluids, **6** (1963) 394.

Deneef C.P., Degroot J.S., Phys. Fluids, 18 (1977) 1151.

Dragila R., Gamaliy E.G., Phys. Rev. A, 44 (1991) 6828.

Duston D., Clark R.W., Davis J., Phys. Rev. A, **31** (1985) 3220.

Dutson D., Davis J., Phys. Rev. A, **21** (1980) 1664.

Elder F.R., Gurewitsch A.M., Langmuir R.V., Pollock H.C., Phys. Rev., **71** (1947) 829.

Forslund D.W., Kindel J.M., Lee K., Phys. Rev. Lett., **39** (1977) 284.

Giulietti D., Biancalana V., Batani D., Giulietti A., Gizzi L., Nocera L., Schifano E., Nuovo Cimento, **13** D (1991) 845.

Glibert K.M., Anthes J.P., Gusinow M.A., Palmer M.A., Whitlock R.R., Nagel D.J., J. Appl. Phys., **51** (1980) 1449.

Kentech Instruments Ltd. Hall Farm Workshops, Didcot (UK), 1992
Kilkenny J.D., Laser Part. Beams **9**, 49 (1991).

Kilkenny, 1991

Kirz J. et al, X-ray data boklet, Lawrence Berkeley Lab. Rep. No. PUB-490 Rev. (1986)

Kruer L., The Physics of Laser Plasma Interactions (Addison Wesley, New York) 1988.

Kruer W.L, Bull. Am. Phys. Soc., **21** (1976) 1048.

Kruer W.L. (1977)

Landen O.L., Campbel E.M., Perry M.D., Opt. Comm., **63** (1987) 253.

Langdon A.B., Phys. Rev. Lett., **44** (1980) 575.

Lawrence Berkeley Lab. Rep. No. PUB-5172 Rev. (1986)

Macchi M., Giulietti D., Bastiani S., Giulietti A., Gizzi L., Nuovo Cimento D, **18** (1996) 727.

Malone R.C., Mc. Crory R.L., Morse R.L., Phys. Rev. Lett., **34** (1975) 751.

Manheimer W.M., Klein H.H., Bull. Amer. Phys. Soc., **19** (1974) 920.

Martin (1980)

Matthews D.L. et al, J. Appl. Phys., **54** (1983) 4260.

Mochizuki T., Yamanaka C., Proc.SPIE, **733**, (1987) 23.

O'Neil F., in Laser-plasma interactions 4, Proceedings of the thirty-fifth Scottish universities'Summer Scool in Physics, St. Andrews (1988)

Rocklett D., Bird C.R., Hailey C.J., Sullivan D., Brown D.B., Burkhalter P.G., Appl. Optics, **24** (1985) 2536.

Spitzer L., Physics of fully ionized gases (Interscience, New York) 1962.

Tooman T.P., Proc. SPIE, **664** (1986) 186.

Willi O., in Laser-Plasma Interactions 4, Proceedings of the 35th Scottish Universities' Summer School in Physics, Edited by M.B. Hooper, (1988).

Wiza L., Nuc. Instrum. and Methods, **162** (1979) 587.

Yaakobi B. et al., Opt. Comm., **38** (1981) 196.